HHS Public Access

Author manuscript

Nat Immunol. Author manuscript; available in PMC 2023 June 22.

Published in final edited form as:

Nat Immunol. 2021 December ; 22(12): 1524–1537. doi:10.1038/s41590-021-01060-7.

Dynamic CD4+ T cell heterogeneity defines subset-specific suppression and PD-L1-blockade-driven functional restoration in chronic infection

Laura M. Snell[1,2,✉], **Wenxi Xu**[1], **Diala Abd-Rabbo**[1], **Giselle Boukhaled**[1], **Mengdi Guo**[1,3], **Bethany L. Macleod**[1], **Heidi J. Elsaesser**[1], **Kebria Hezaveh**[1], **Nirmin Alsahafi**[1], **Sabelo Lukhele**[1], **Sara Nejat**[4], **Ramanandan Prabhakaran**[1], **Slava Epelman**[3,4,5], **Tracy L. McGaha**[1,3], **David G. Brooks**[1,3,✉]

[1]Princess Margaret Cancer Centre, University Health Network, Toronto, ON, Canada.

[2]Department of Microbiology and Immunology, Indiana University School of Medicine, Indianapolis, IN, USA.

[3]Department of Immunology, University of Toronto, Toronto, ON, Canada.

[4]Toronto General Hospital Research Institute, University Health Network (UHN), Toronto, ON, Canada.

[5]Peter Munk Cardiac Centre, Ted Rogers Centre for Heart Research, Toronto, ON, Canada.

Abstract

Inhibiting PD-1:PD-L1 signaling has transformed therapeutic immune restoration. $CD4^+$ T cells sustain immunity in chronic infections and cancer, yet little is known about how PD-1 signaling modulates $CD4^+$ helper T (T_H) cell responses or the ability to restore $CD4^+$ T_H-mediated immunity by checkpoint blockade. We demonstrate that PD-1:PD-L1 specifically suppressed $CD4^+$ T_H1 cell amplification, prevents $CD4^+$ T_H1 cytokine production and abolishes $CD4^+$

✉ **Correspondence and requests for materials** should be addressed to Laura M. Snell or David G. Brooks. lausnell@iu.edu; dbrooks@uhnresearch.ca.

Author contributions

L.M.S. and D.G.B. designed the research. L.M.S., W.X., M.G., B.L.M., H.J.E., S.L., K.H. and N.A. performed the experiments. L.M.S., D.A.-R., G.B., S.N., and R.P. analyzed the data. S.E. and T.L.M. contributed technical expertise and discussion. L.M.S. and D.G.B. wrote the paper.

Online content

Any methods, additional references, Nature Research reporting summaries, source data, extended data, supplementary information, acknowledgements, peer review information; details of author contributions and competing interests; and statements of data and code availability are available at https://doi.org/10.1038/s41590-021-01060-7.

Competing interests

The authors declare no competing interests.

Additional information

Extended data is available for this paper at https://doi.org/10.1038/s41590-021-01060-7.

Supplementary information The online version contains supplementary material available at https://doi.org/10.1038/s41590-021-01060-7.

Peer review information *Nature Immunology* thanks Robert Thimme, Santosha Vardhana and the other, anonymous, reviewer(s) for their contribution to the peer review of this work. L. A. Dempsey was the primary editor on this article and managed its editorial process and peer review in collaboration with the rest of the editorial team.

cytotoxic killing capacity during chronic infection in mice. Inhibiting PD-L1 rapidly restored these functions, while simultaneously amplifying and activating T_H1-like T regulatory cells, demonstrating a system-wide CD4–T_H1 recalibration. This effect coincided with decreased T cell antigen receptor signaling, and re-directed type I interferon (IFN) signaling networks towards dominant IFN-γ-mediated responses. Mechanistically, PD-L1 blockade specifically targeted defined populations with pre-established, but actively suppressed proliferative potential, with limited impact on minimally cycling TCF-1^+ follicular helper T cells, despite high PD-1 expression. Thus, $CD4^+$ T cells require unique differentiation and functional states to be targets of PD-L1-directed suppression and therapeutic restoration.

Robust effector T cell responses are critical to the resolution of viral infection and when compromised, chronic infection ensues. At the onset of what will become a chronic viral infection, sustained antigen signaling remodels the immune environment, driving the production of immunosuppressive cytokines and the expression of multiple inhibitory receptors/ligands that further potentiate viral persistence (for example, IL-10, PD-1, PD-L1, Tim3). This immunosuppressive program diminishes CD8 T cell function (termed T cell exhaustion) and maintains virus-specific T cells in an attenuated functional and distinct epigenetic state that is unable to eliminate infection[1]. Characteristics of cellular and molecular exhaustion are also observed in T cells during cancer, indicating a conserved program of T cell dysfunction in response to chronic antigen stimulation. Further exacerbating cell-intrinsic CD8 T cell dysfunction in chronic infection is the progressive loss of virus-specific $CD4^+$ type 1 helper T cells (T_H1) and the reciprocal accumulation of B cell helping $CD4^+$ follicular helper T cells (T_{FH}) as virus persists[2–5]. Although the exhausted state of CD8 T cells is relatively well-defined, the cellular and molecular changes that comprise $CD4^+$ T cell functional alterations in chronic infection and cancer are little understood. Further adding to this complexity is the multiple T_H differentiation states that $CD4^+$ T cells progress toward, leading to the unique requirement to consider functional changes in molecular programs within the context of specific T_H differentiation states. $CD4^+$ T_H1 cell help is critical to sustain CD8 T cells during viral persistence, and the progressive $CD4^+$ T_H1 loss promotes CD8 T cell exhaustion and defective viral control[6]. Therapeutically, transfer of virus-specific $CD4^+$ T_H1 cells in the middle of an established chronic infection increased antiviral CD8 T cell numbers and function to enable viral control[6]. Thus, the loss of $CD4^+$ T_H1 cells is a critical mechanism promoting CD8 T cell dysfunction, and enhancing this distinct virus-specific $CD4^+$ helper T cell subset can overcome CD8 T cell exhaustion to increase immune control of chronic infections.

Immunotherapy that blocks inhibitory receptors/ligands to reverse T cell exhaustion and enhance immune function has spurred a revolution in treating chronic disease. Among the most successful of these immunotherapies has been the blockade of the PD-1:PD-L1 (PD-1/L1) pathway. PD-1/L1 blockade enhances CD8 T cell function in many viral infections, including chronic lymphocytic choriomeningitis virus (LCMV), HIV, HCV; in numerous preclinical cancer models, and has been particularly successful in a subset of cancer patients[1]. Because CD8 T cells are critical effectors of viral and tumor clearance, the bulk of the work studying the effects of anti-PD-1/L1 therapy has focused on their role. Indeed, a distinct TCF-1^+ memory-like CD8 T cell subset has been identified as

the specific CD8 T cell population targeted by the PD-1/L1-blocking therapy[7–13]. Yet, in certain instances, patients respond to anti-PD-1/ L1 blockade independent of CD8 T cell responses[14,15], indicating that many cell types are likely responding to and affecting the outcome of this therapy than previously recognized.

PD-1 can be highly expressed on activated $CD4^+$ T cells, suggesting that these T cells may also be responsive to PD-1/L1-blocking therapies. Although blocking PD-1/L1 is not widely considered to target $CD4^+$ T cells[16], increasing evidence in patients suggests that, at least in some instances, $CD4^+$ T cells can respond to this therapy[14,17]. The reason underlying these discrepancies in how or why $CD4^+$ T cells may (or may not) respond to PD-1/L1-blocking immunotherapy is unclear, but may be explained by differences in precursor $CD4^+$ helper T cell populations. For instance, if anti-PD-1/L1 specifically targets distinct types of $CD4^+$ helper T cell subsets, the therapy will likely be effective only in cases in which these specific helper T cell subsets are present pretreatment. Yet to date, a precise role of PD-1/L1 blockade in restoring $CD4^+$ T cell responses and the potential for differential helper T cell subset targeting remains unclear.

Results

Virus-specific $CD4^+$ T cell heterogeneity during chronic infection.

To investigate how exhausted $CD4^+$ T cells are affected by anti-PD-L1 therapy during chronic viral infection, LCMV-glycoprotein $(GP)_{61–80}$-specific $CD4^+$ T cell antigen receptor (TCR) transgenic (SMARTA) T cells were adoptively transferred into naïve mice that were subsequently infected 1 day later with LCMV clone 13 (Cl13) to generate a chronic infection. The SMARTA T cells, all expressing the same TCR, functionally and phenotypically recapitulate host-derived endogenous $GP_{61–80}$-specific $CD4^+$ T cells[2,18,19], and are used to control for inherent differences in strength of TCR signaling in the total population. Twenty-five days after infection, mice were treated with either anti-PD-L1-blocking antibody or isotype control antibody and were continued on this treatment regimen every 3 days. SMARTA cells were analyzed after the first and third treatments and co-clustered based on time-of-flight mass cytometric (CyTOF) staining (Extended Data Fig. 1a and Supplementary Tables 1 and 2). PD-L1 blockade did not alter viral titers following one treatment, but in this experiment decreased viral titers were observed after three treatments (Extended Data Fig. 2a). All the $CD4^+$ SMARTA T cells are primed early after infection[20], are activated throughout infection and exhibited high PD-1 expression at the start of the treatment. Analysis revealed that the SMARTA T cells formed ten distinct clusters that could be broadly grouped into those that expressed the transcription factor TCF-1 (c1–5, c7 and c10) and those that did not (c6, c8 and c9) (Fig. 1a,b). TCF-1 drives expression of the T_{FH} transcriptional regulator Bcl-6 (refs. [21,22]), and is absent in T_H1 cells. Consistent with this, TCF-1-negative c6, c8 and c9 had very low expression of Bcl-6 and expressed multiple T_H1 cell-associated proteins. In c8 and 9, these included GzmB, Eomes, as well as Tim3 and CD39 (inhibitory receptors that are highly expressed on T_H1 cells), whereas c6 had high expression of T-bet (a transcription factor driving T_H1 differentiation) and SLAMF1 (an activation marker defining T_H1 cells in LCMV infection). Of the T_H1 clusters, c8 was unique in that it expressed the T_H1 chemokine receptor CX3CR1 and appeared to be more

terminally differentiated with a higher proportion of cells expressing Tim3 and GzmB, and the highest expression of CD80 and Lag3 (Fig. 1a). Thus, c6, c8 and c9 were residual T_H1 clusters sustained during chronic viral infection, with c6 a potentially less-differentiated T_H1 population and c8 the most terminally differentiated.

Of the TCF-1^+ clusters, c2 exhibited the highest expression of Bcl-6, CXCR5, ICOS, Helios and was uniquely positive for CD69, suggesting the most differentiated T_{FH} cells (Fig. 1a, b). Although all the $CD4^+$ SMARTA cells were activated and expressed high levels of PD-1, the T_{FH} c2 along with the T_H1 clusters expressed the highest levels of PD-1, suggesting that these clusters were the most highly activated. The other TCF-1^+ clusters c1, c3, c4, c5, c7 and c10 expressed IL-7Rα (CD127), and potentially signify less antigen-engaged, less terminally differentiated cells. Even among the less-differentiated/less-activated $CD127^+$TCF-1^+ clusters, substantial heterogeneity existed suggestive of hybrid T_H1/T_{FH} cells. For instance, c1, c4, c5 and c7 had high TCF-1 expression, but simultaneously expressed T-bet and some SLAMF1. Cluster 10, on the other hand, appeared to favor neither the T_H1 or T_{FH} lineages and had the highest expression of CD127, likely being the least differentiated of all the clusters. Thus, extensive heterogeneity exists amongst $CD4^+$ T cells during chronic viral infection, and in addition to T_H1 and T_{FH}, multiple hybrid clusters emerge that have characteristics of both T_H1 and T_{FH} cells.

PD-L1 blockade restores virus-specific $CD4^+$ T_H1 cells.

PD-L1 blockade increased the proportions of the T_H1 clusters (6, 8, 9), and drove a smaller increase in the proportion of c3, while decreasing the proportion of the TCF-1^+ intermediate c4 (Fig. 1a and Extended Data Fig. 2b). The overall number of SMARTA T cells was elevated ($p = 0.06$) following the initial treatment (Extended Data Fig. 2c), primarily as a result of the increased T_H1 clusters, and to a lesser extent from an increase in c3 and c1 (a transitional cluster associating next to the T_H1 cells in UMAP space) (Fig. 1c). Gating on endogenous Foxp3−, PD-1^+CD4^+ T cells revealed that the T_H1, but not TCF-1^+ cells were also increased following anti-PD-L1 treatment, confirming that this was not an epitope, TCR or transgenic specific effect (Extended Data Fig. 2d). Unlike T_H1 cells, the proportion and absolute number of the most differentiated T_{FH} c2 was largely unaffected by PD-L1 blockade at this early timepoint, despite the high levels of PD-1 expression (Fig. 1a–c and Extended Data Fig. 2b). Direct comparison within the same mouse further revealed that the fold changes were significantly higher in the T_H1 cells following PD-L1 blockade compared with the small increases observed in the T_{FH} cluster (Fig. 1d). Functionally, anti-PD-L1 blockade increased IFN-γ-producing virus-specific $CD4^+$ T cells, as well as the amount of IFN-γ produced per cell, while simultaneously increasing virus-specific $CD4^+$ T cells producing IL-10 (Fig. 1e and Extended Data Fig. 2e), suggesting a negative feedback inhibition induced by the enhanced stimulation, but also consistent with observations that IL-10 production is specifically produced by T_H1 cells during chronic viral infection[23]. On the other hand, there was no difference in the proportion or numbers of TNF-producing virus-specific $CD4^+$ T cells (Fig. 1e and Extended Data Fig. 2e), indicating that not all cytokines were enhanced by blocking PD-L1. PD-1-deficient virus-specific $CD4^+$ T cells also exhibited significantly increased T_H1 differentiation by both proportion and number, as well as enhanced IFN-γ production, with only minimal effects on T_{FH} numbers (Fig.

1f), thus demonstrating the $CD4^+$ T cell-intrinsic nature of PD-1 signaling is to inhibit T_H1 expansion and function throughout chronic viral infection.

After three anti-PD-L1 treatments (8 days after the initiation of treatment and 33 days after infection), there was a numerical increase in the majority of $CD4^+$ SMARTA T cell clusters in the PD-L1 blocked mice, corresponding to the maintenance of these cells between these treatments (Extended Data Fig. 2f). Further, the number of IFN-γ and IL-10 expressing cells remained elevated following three anti-PD-L1 treatments (Fig. 1g). PD-L1 blockade also increased numbers of $CD4^+$ T_H1 SMARTA cells in the liver and lungs following three treatments, and although Bcl-6hi T_{FH} populations were not present in these nonlymphoid organs, the population of Bcl-6lo TCF-1^+ cells was less responsive to PD-L1 blockade (Extended Data Fig. 2g). Thus, anti-PD-L1 specifically increases the proportion and number of virus-specific $CD4^+$ T_H1 cells in both lymphoid and nonlymphoid organs.

Blocking PD-L1 targets precycling $CD4^+$ T_H1 populations.

To determine the origin of the increased T_H1 cells following PD-L1 blockade, we examined the trajectory of virus-specific $CD4^+$ T cells following anti-PD-L1 treatment. Overlaying the UMAP clusters onto a diffusion pseudotime map[24] revealed three tips (T), which form the most distant endpoints of each branch and indicate the beginning or end of a differentiation state (Fig. 2a and Extended Data Fig. 3a). T1 was a T_{FH} cell in c2; T2 was a cell from the most differentiated T_{H1} c8; and T3 was a cell in the immature/transitional SLAMF1^+ T_{H1} c6. Pseudotime diffusion analysis identified two branches that mapped from the central SLAMF1^+ T_H1 cell T3 root, where it could either progress towards the T_{FH} fate (as nor mally occurs during chronic viral infection as T_H1 cells convert to T_{FH})[2], or towards more differentiated T_H1 clusters. To identify which of these directions was favored by PD-L1 blockade, we overlaid changes in cell number following anti-PD-L1 treatment onto the diffusion pseudotime map. Blocking PD-L1 rapidly increased both the proportion and numbers of the clusters on the branch towards the highly differentiated T_H1 c8 in T2 (Fig. 2a), suggesting that anti-PD-L1 diverts $CD4^+$ T cells from the normal T_{FH} differentiation branch in chronic infection and can push less-committed T_H1 cells towards the differentiated T_H1 lineage.

PD-L1 blockade rapidly increased the proportion and the number of $Ki67^+$ (that is, cycling) virus-specific $CD4^+$ T cells (Fig. 2b and Extended Data Fig. 3b). The vast majority of $Ki67^+$ cells in the isotype-treated group (representing pretherapy) were in the T_H1 c6 and c8, and the T_H1-associating c1 (Fig. 2c). Critical for these analyses, the SMARTA cells were not clustered using Ki67 to prevent algorithmic clustering of cycling cells (Supplementary Table 2). Although the frequency of $Ki67^+$ cells increased following PD-L1 blockade (Fig. 2b), the distribution of clusters that expressed Ki67 was generally unchanged (Fig. 2c). The exception to this was the T_H1 c9, which exhibited low Ki67 expression in isotype-treated mice, but was robustly induced by anti-PD-L1 treatment (Fig. 2c). The increase in c9 is consistent with the pseudotime trajectory analysis indicating that activated cells in c6 progress through c9 toward the most differentiated population of T_H1 cells in c8. Conversely, c8 started out with the highest frequency of $Ki67^+$ cycling cells and this was then maintained following anti-PD-L1 therapy. Whereas the frequency of $Ki67^+$ cells in T_{FH}

c2 and intermediates c4 and c5 were also enhanced upon PD-L1 blockade (Fig. 2c), the proportion of these cells remained small, and did not lead to an increase in the absolute numbers of those clusters, as was observed for the T_H1 clusters (Fig. 1c).

The majority of $Ki67^+$ cells in both isotype and anti-PD-L1 treated mice similarly expressed T_H1 proteins CD39, T-bet and SLAMF1, and largely failed to express CD69 (Fig. 2d), a protein specifically on the c2 T_{FH}. Further, the $Ki67^+$ SMARTA cells in both isotype and anti-PD-L1 treated mice exhibited highly overlapping protein expression patterns with each other, and were more similar to each other than to their respective Ki67-negative cells (Fig. 2e and Extended Data Fig. 3c), further suggesting anti-PD-L1 blockade preferentially expands pretreatment cycling clusters. Even early in infection (day 10 after LCMV-Cl13 infection), Ki67 was predominantly confined on to the T_H1 c4, c6, whereas the majority of $TCF\text{-}1^+$ clusters, and particularly the most differentiated T_{FH} subset c1, expressed less Ki67 (Extended Data Fig. 3d). Thus, PD-1 limits the expansion of the most proliferative $CD4^+$ T_H1 cell subset throughout chronic infection, and blocking PD-L1 overcomes these constraints.

PD-L1 blockade targets T_H1-phenotype T regulatory cells.

$Foxp3^+$ T_{reg} cells comprise approximately 20% of total $CD4^+$ T cells during chronic viral infection and can differentiate into different Th-like subsets to suppress antiviral responses[25]. Importantly, SMARTA cells in LCMV infection do not become T_{reg} cells[20], although in other infections virus-specific $CD4^+$ T cells potentially could. The frequency of T_{reg} cells rapidly increased after the first anti-PD-L1 treatment compared with isotype-treated mice and PhenoGraph clustering revealed eight distinct clusters that again broadly categorized into $TCF\text{-}1^+$ (c1, c3, c4, c7, c8) and TCF-1-negative (c2, c5, c6) populations, with the TCF-1-negative T_{reg} cells expressing T-bet to both higher levels and in a larger proportion of cells (Fig. 3a,b and Supplementary Table 3). PD-L1 blockade did not numerically affect the $TCF\text{-}1^+$ clusters, but increased the TCF-1-negative, T_H1-like c2, c5, c6 (Fig. 3b,c and Extended Data Fig. 4a,b). Although all T_{reg} cells were gated based on Foxp3 positivity (Extended Data Fig. 1b), Foxp3 expression itself, along with T_H1-associated inhibitory receptors CD39 and Tim3, as well as activation markers CD27, CD44 and SLAMF1 were all enriched in the T_H1-phenotype clusters (Fig. 3b). These T_H1 clusters also had the highest expression and contained the majority of $ICOS^+$, $CTLA4^+$ and $PD\text{-}1^+$ cells, demonstrating heightened activation of the T_H1-phenotype T_{reg} cells during chronic infection.

PD-L1 blockade also rapidly increased the expression of multiple activation/inhibitory proteins (including CTLA4, ICOS, CD80, CD86, SLAMF1) on the T_H1-phenotype clusters compared with isotype treatment (Fig. 3d). Although anti-PD-L1 therapy did not bolster the number of $TCF\text{-}1^+$ T_{reg} cells, it did increase their expression of proteins such as PD-1, Helios, SLAMF1, ICOS and CTLA4 on multiple clusters (Fig. 3d), indicating that these populations were also being affected by the therapy. The inhibitory receptor CTLA4 was upregulated on multiple T_{reg} cell clusters following anti-PD-L1 (c2–5, c8), but it had much lower/nondetectable expression on the virus-specific $CD4^+$ T cells. T_{reg} cell depletion led to increased numbers of $CD4^+$ T_H1 cells, but not T_{FH} cells, with a particular restoration

of $GzmB^+CD4^+$ T_H1 cells (Extended Data Fig. 4c), indicating that consistent with their activated T_H1-phentoype, T_{reg} cells in the chronic infection preferentially suppress T_H1 responses.

At baseline and following PD-L1 blockade, a higher proportion of T_{reg} cells expressed Ki67 than did the virus-specific $CD4^+$ T cells (Fig. 3e). PhenoGraph clustering was performed in the absence of Ki67 (Supplementary Table 3), and again, the $Ki67^+$ cycling cell clusters at the onset of therapy were predominantly confined to the T_H1-like T_{reg} cells (c2, c5) (Fig. 3f). The cycling clusters that were present pretherapy (that is, in isotype-treated mice) were generally also the ones that were expanded by anti-PD-L1, and although an increase in the frequency of $Ki67^+$ cells also occurred in T_{reg} clusters c3, c6 and c8 (Fig. 3f), only the T_H1-like c2, c5 and c6 were increased numerically (Fig. 3c and Extended Data Fig. 4a). Comparison of the $Ki67^+$ cells in isotype and anti-PD-L1 conditions showed that cycling T_{reg} cells exhibited similar protein expression patterns, with the vast majority of $Ki67^+$ T_{reg} cells expressing T-bet, ICOS and CTLA4, and high CD39, whereas the majority of the cycling cells in both conditions failed to express TCF-1 and CD69 (Fig. 3g). The similar overall protein expression patterns by cycling cells in isotype- and anti-PD-L1 treated mice suggested that specific pre-established populations of cycling virus-specific $CD4^+$ T_H1 cells and T_H1-like T_{reg} cells are specifically expanded by PD-L1 blockade.

Following the third anti-PD-L1 treatment, the number of total and T_H1-phenotype T_{reg} cells had contracted to the same level as in isotype-treated mice (Fig. 3h and Extended Data Fig. 4d). Yet, PD-L1 blockade continued to drive higher levels of activation proteins, particularly in T_H1-like c2, c5 and c6, whereas the $TCF\text{-}1^+$ T_{reg} cells appeared to be only minimally changed (Extended Data Fig. 4e). Despite the contraction, the T_H1-like c2 and c5 still comprised the majority of the $Ki67^+$ cells in both isotype and anti-PD-L1 groups, although the proportions of $Ki67^+$ cells within these T_H1 clusters were no longer significantly elevated in response to PD-L1 blockade (Extended Data Fig. 4f). Like the cycling virus-specific $CD4^+$ T cell populations, the $Ki67^+$ cells following the first and third anti-PD-L1 treatments had concordant protein expression patterns both between time points, and between isotype and anti-PD-L1 treatment (Fig. 3i and Extended Data Fig. 4g), indicating that like the virus-specific $CD4^+$ T cells, the T_H1-like T_{reg} cells are targeted by PD-1/PD-L1 to limit their expansion and activation state.

T_{reg} cells in nonlymphoid organs (the liver and lung) increased following three anti-PD-L1 treatments, at a time when T_{reg} cell amplification in the spleen had returned to baseline (Fig. 4a). To determine whether this increase was the result of local proliferation versus an influx of T_{reg} cells from the lymphoid organs, we treated mice just before and then during anti-PD-L1 treatment with the drug FTY720 (fingolimod) to prevent cell emigration from lymphoid tissue. FTY720 treatment reduced T_{reg} cells in the isotype conditions (Fig. 4b), suggesting that ongoing T_{reg} cells in the lung and liver during chronic infection are replenished by homing from lymphoid organs. Yet, even with FTY720 treatment, PD-L1 blockade expanded the number of T_{reg} cells in the liver and lung (Fig. 4b). Further, PD-L1 blockade increased T_{reg} cell infiltration into the liver and lung tissue parenchyma, and within the spleen from the red pulp to the white pulp[26] (Fig. 4c). Thus, PD-L1 blockade expands T_{reg} cells directly in nonlymphoid organs, and functions to amplify T_{reg} presence within

the tissue parenchyma of these organs, where they are potentially positioned to interact and suppress effector T cells.

Gene expression changes by virus-specific CD4$^+$ T cells following PD-L1 blockade.

We next performed single-cell RNA-sequencing (scRNA-seq) on SMARTA T cells following isotype or anti-PD-L1 treatment. Analysis was performed after the third antibody treatment to allow for network redistributions to take hold, while viral titers were not yet decreased by PD-L1 blockade in this particular experiment (Extended Data Fig. 5a). Cell-cycle genes were regressed out before clustering (akin to clustering CyTOF data without Ki67). Of the eight clusters that emerged, only c2 and c3 increased following anti-PD-L1 blockade and these were characterized by expression of T_H1-cell genes, including *Ifngr*, *Ifng*, *Gzmb*, *Ccl5*, *Selplg* (encoding PSGL1) and *Nkg7* (Fig. 5a–c). c3 was a highly differentiated T_H1 cluster (corresponding to c9 and some of c8 in the CyTOF analysis Fig. 1), and exclusively expressed *Prdm1* (encoding Blimp1) and had the majority of *Gzmb* expression (Fig. 5c). *Tcf7* (encoding TCF-1) was widely expressed by most clusters, but was largely absent from c3 and only present in the proportion of c2 that lacked *Gzmb* expression (Fig. 5c), suggesting c2 is a transitional population containing cells further differentiating to T_H1, akin to c1 and c6 in the CyTOF clustering. All clusters were activated, although c0 was the least differentiated cluster, expressing *Il7ra* (CD127), *Tcf7* and *Ccr7*, characteristic of more quiescent cells (Fig. 5b,c). c5 was comprised of bona fide T_{FH} cells expressing *Ascl2, Bcl-6* and *Cxcr5*, whereas c1 was composed of cells expressing T_{FH}-associated genes, but not their lineage-defining transcription factors, thus we defined these as less-differentiated T_{FH}. c7 expressed high amounts of IFN-stimulated genes (ISGs), and seemed to encompass both T_H1 and T_{FH} cells, indicating clustering was driven by the ISG signature and not a specific differentiation program. c6 had high expression of the genes *Xcl1, Slamf7*, *Tnfrsf9* and *Crtam*, and appeared to be a hybrid between T_H1 and T_{FH}, expressing molecules such as *Gzmk* and *Runx3*, but also *Tcf7*, *Sostdc1* and *Bcl-6*.

When all the clusters were combined, there were 461 significantly differentially expressed genes (DEG) following PD-L1 blockade (adjusted $P < 0.05$) (Supplementary Table 4). However, none increased more than twofold, and only *Rps18-ps3*, (ribosomal protein S18 pseudogene 3), and three predicted genes (*Gm6133*, *Gm98433*, *Gm2000*) reached twofold decreases upon blockade, indicating that at the population level the cells were transcriptionally similar following therapy. Of the DEG in the total SMARTA cell population, there was an overall increase in T_H1 signature genes following PD-L1 blockade, including *Nkg7*, *Ccl5*, *Selplg* and *Lgals3*, which was accompanied by a global decrease in T_{FH} signature genes including *Sostdc1*, *Tnfsf8* (encoding CD30L), *Tcf7*, *Izumo1r* (encoding for JUNO), *Il21* and *CD40lg* (Fig. 5d, Extended Data Fig. 5b). The decreased T_{FH} signature gene expression also occurred within the T_{FH} and T_{FH}-like clusters, suggesting that despite a lack of expansion, the nature of these cells was also being fundamentally altered (Supplementary Table 4). Along with the diminished T_{FH} gene expression, PD-L1 blockade decreased *Il21* production (a factor critical for control of chronic viral infection[19,27,28]), which was produced by both T_H1 and T_{FH} in isotype conditions and now had only minimal residual expression in T_{FH} phenotype cells (Fig. 5d). Although the decreased T_{FH} gene signature was evident across all SMARTA cell clusters following PD-L1 blockade, the

increase in T_H1 driving genes was largest in c2 (the transitional T_H1 cluster) and in some cases the less-differentiated, centrally located c0. c2 itself expressed 64 DEG in anti-PD-L1 versus isotype treatment, with more than twofold increased expression of T_H1-associated genes, including *Plac8*, (placenta specific 8) *Ctla2a* (cytotoxic T lymphocyte-associated protein 2 alpha), *Klrd1* (killer cell lectin like receptor D1) and *Ly6c2*, as well as *Nkg7* and *Lgals3* (encoding galectin3) (Fig. 5e and Extended Data Fig. 5b). c0 and c1 expressed 140 and 68 DEG respectively, whereas clusters 3–7 expressed fewer than 40 DEG each (Supplementary Table 4). Many of the DEG in c0 and c1 were ribosomal proteins that were downregulated upon PD-L1 blockade. T_H1 genes were also upregulated in these clusters upon PD-L1 blockade (particularly c0) with genes such as *Nkg7*, *Ccl5* increased in c0 and c1, and genes such as *Sostdc1*, *Tnfsf8* (encoding CD30L), *Tnfrsf4* (encoding OX40) and *Il21* decreased in c0 (Supplementary Table 4). In addition, anti-PD-L1 therapy increased *Il7ra* and *Bcl2* expression in c0, suggesting enhanced cell survival of this less-differentiated population that likely were precursors to T_H1 cells. Thus, not only were T_H1 clusters enhanced by proportion and number by PD-L1 blockade, but there was a system-wide recalibration towards the T_H1 differentiation state.

To analyze the transcriptional programs pushing the transition of the T_H1 cells, we compared the genes differentially regulated from the transitional T_H1 c2 with the terminally differentiated T_H1 c3. Compared with c2, c3 exhibited increased expression of multiple T_H1 defining and modulating genes, including increased expression of *Ifng* and multiple inhibitory receptors, including *Lag3*, *Pdcd1* and *Entpd1* (encoding CD39) (Fig. 5f and Extended Data Fig. 5c). Further, c3 was the only cluster that produced *Il10* (Extended Data Fig. 5c), indicating feedback inhibition by the most terminally differentiated T_H1 cells. PD-L1 blockade itself did not directly enhance these genes in c3 compared with isotype, indicating instead that PD-L1 directed the less-differentiated T_H1 cells down a terminal differentiation pathway leading up to c3. The expression of transcription factor *Tox* (which drives CD8 T cell exhaustion[29–31]), *Eomes* (which associates with exhausted CD8 T cells[32]) and *Maf* which can drive *Il10* expression[33] were increased in c3 compared with c2 (Fig. 5f), indicating that the transcriptional transformations associated with CD8 T cell exhaustion underlay the transition to $CD4^+$ T_H1 terminal differentiation during chronic infection.

Network profiling reveals global transcriptional changes.

We next measured putative upstream regulators of DEGs in total cells, and focused on the T_H1 c2 and c3, as well as the T_{FH} c5, to understand how blocking PD-L1 modified the downstream T_H1 and T_{FH} cell transcriptional programs. Upstream regulator analysis predicted PD-L1 blockade-induced activation of central T_H1 differentiation networks (for example, Tbx21, Id2, Tet2, IRF4), and inhibition of T_{FH} driving cytokine networks (IL6, IL27, IL21, STAT3) (Fig. 6a). These occurred in conjunction with the predicted downregulation of T_{FH}-associated regulators CD40lg and CD28 in c5, and the predicted activation of multiple upstream regulators for networks that control cellular proliferation (for example, Myc, Mycn, Itk, Ccnd1), particularly in c2. Chronic IFN-I signaling suppresses antiviral $CD4^+$ T cell proliferation and function in chronic viral infection[34,35], and multiple IFN-I related upstream regulators (IFN-α/β, IFN-α1/ IFN-α13, IFN-α2, IFN-αR1, JAK1/2) were predicted to be inhibited upon PD-L1 blockade in both T_H1 and T_{FH} clusters, whereas

regulation through the SOCS1 network, an inhibitor of IFN-I signaling, was predicted to be elevated in the transitional T_H1 population c2, as well as the T_{FH} population c5. In line with diminished IFN-I mediated regulation, PD-L1 blockade decreased expression of numerous ISGs, such as *IRF7* and *OAS1a*, while reciprocally elevating T_H1-driving ISGs, such as *Ccl5* and *Ifngr* (Fig. 6b and Extended Data Fig. 6a). Unexpected with the increased cycling and activation states of virus-specific $CD4^+$ T_H1 cells following PD-L1 blockade, TCR signaling (TCR, CD3, NR4A1 (encoding Nur77)) and multiple key immune-activating signaling pathways induced by TCR signaling (NFATC, RICTOR, NFKB) were predicted to be inhibited by PD-L1 blockade. Deeper examination revealed downregulation of many TCR-stimulated transcription factors by PD-L1 blockade (Fig. 6c), corresponding to a global diminution of TCR signaling strength when PD-L1 is inhibited. Only a few TCR-driven transcription factors were increased following PD-L1 blockade, particularly in the transitional T_H1 c2, and these were specifically associated with T_H1-fate determination and included *Prdm1* and *Klf2*, as well as *Tsc22d3* which is stimulated by IL-10 (Fig. 6c). Further, Nur77 protein expression, which is directly associated with the strength of TCR signaling[36], was decreased rapidly (and before decrease in viral titers) in virus-specific $CD4^+$ T cells from anti-PD-L1 treated compared with isotype-treated mice (Fig. 6d and Extended Data Fig. 6b). Both heightened and chronic TCR signaling promote conversion of T_H1 to T_{FH} cells[2,37], suggesting that blocking PD-L1 reduces TCR signaling networks to re-establish T_H1 programming.

To further probe anti-PD-L1 mediated changes in transcription factor activity and their downstream target gene networks, we used the algorithm SCENIC (single-cell regulatory network interference and clustering)[38]. SCENIC identifies each transcription factor and its direct binding targets in the same cell (termed regulons) based on coexpression profiles and cis-regulatory motif enrichment. Quantification of the fold change in average regulon activity indicated that the decreased expression by scRNA-seq of multiple transcription factors involved in TCR signaling following PD-L1 blockade corresponded to a similar decrease in their target RNAs (regulons), including regulons driven by Fos, Jun, Nfatc1, Maf and Relb (Fig. 6e). The T_{FH} c5 had a generally higher activity score for many of these regulons than the T_H1 clusters during chronic infection, consistent with strong TCR signaling driving the T_{FH} phenotype. Yet, even in this T_{FH} c5, target regulons driven by Fos, Hif1a and Nfatc1 were significantly decreased upon anti-PD-L1 therapy. Although *Eomes* RNA was decreased following PD-L1 blockade, its target regulons remained elevated in c2 and c3, suggesting a delay in the transcriptional decrease in its expression and the functional activity of the protein. Conversely, the increased expression of *Prdm1* following PD-L1 blockade was mirrored in increased expression of its target regulons, further corroborating the re-enforcement of T_H1-like genes programing.

Pathway analysis of the individual cell clusters indicated enrichment of pathways involved in positive regulation of translation, RNA splicing, cell cycling and cellular metabolic processes when PD-L1 was inhibited (Extended Data Fig. 6c), indicating metabolic reprogramming of virus-specific $CD4^+$ T cells. Corresponding to the overall virus-specific $CD4^+$ T cell survival observed following PD-L1 blockade, stress response pathways such as "*response to cold*", and pathways of negative regulation of apoptosis were increased across most of the clusters. Specifically, within the less-differentiated $CD4^+$ T_H1 c2, but not

the terminally differentiated T_H1 c3, PD-L1 blockade amplified multiple pathways involved in DNA replication and cell-cycle progression, further indicating cell-intrinsic modulation of cell-cycle machinery fueling expansion of the T_H1 c2 population and c3 arising from these cells. Conversely, following PD-L1 blockade, c3 was enriched for pathways of T_H1 functional activity, regulation of lymphocyte migration, leukocyte-mediated cytotoxicity and decreased STAT3 signaling (STAT3 is known to inhibit T_H1 differentiation[39]) (Fig. 6f). Like the widespread inhibition of upstream regulation by IFN-I, the pathway "*response to interferon-alpha*" was one of the few pathways downregulated in c2 and c3 of the anti-PD-L1 treated group (Fig. 6f). Conversely, both c2 and c3 had increased signatures of IFN-γ activation and signaling, indicating a switch from chronic IFN-I toward IFN-γ signaling in response to PD-L1 blockade. Both c2 and c3 had gene signatures associated with CD8 T cell effector function following anti-PD-L1 therapy (c2 up in "*effector vs exhausted CD8 T cells*"; c3 up in "*leukocyte-mediated cytotoxicity*") (Fig. 6f), suggesting the molecular acquisition of a gene signature pushed toward CD8 T cell effector functions.

PD-L1 blockade drives a CTL gene signature and resurrects CD4$^+$ killing capacity.

The increased signatures of CD8 T cell effector functions and IFN-γ signaling suggested that the TH1 may acquire cytolytic function when PD-L1 signals are inhibited. Indeed, multiple cytotoxic mediators including *Nkg7*, *Runx3* (the transcription factor that drives cytotoxic function in CD8 T cells), *Gzmb, Gzmk, Fasl, Ctla2a, Klrd1 and Klrk1* (encoding NKG2D) were preferentially expressed in T_H1 clusters 2 and 3 (Fig. 7a and Extended Data Fig. 7), and were increased in expression and/or by proportion upon PD-L1 blockade. (Fig. 7b). By contrast, the non-T_H1 clusters lacked or had minimal expression of these cytotoxic mediators and failed to upregulate them (Fig. 7a and Extended Data Fig. 7), suggesting the cytotoxic signature was localized to the T_H1 cells. To directly test whether PD-L1 blockade-induced changes in virus-specific CD4$^+$ T cell cytolytic function, we performed an in vivo CD4$^+$ cytotoxic T lymphocyte (CTL) assay. To ensure killing was mediated by CD4$^+$ T cells and was CD8$^+$ T cell independent, we used β_2-microglobulin (β_2M) deficient splenocytes (that is, lacking MHC class I expression) as target cells. The splenocytes were labeled with LCMV-$GP_{61–80}$ peptide (the SMARTA epitope) or an irrelevant peptide ($OVA_{323–339}$) and then coinjected into LCMV-Cl13 infected mice after the third anti-PD-L1 treatment. Naïve mice demonstrated no specific killing of MHC II$^+$ target cells compared with $OVA_{323–339}$ labeled cells (Fig. 7c). Mice acutely infected with LCMV-Armstrong exhibited approximately 55% specific killing of transferred LCMV-$GP_{61–80}$ labeled MHC II$^+$ target cells, whereas this killing was completely abolished in chronically infected isotype-treated mice. Interestingly, PD-L1 blockade completely restored CD4$^+$ T cell mediated killing to levels observed in the acutely infected mice. The CD4$^+$-mediated killing was MHC class II dependent, as target cells that lacked MHC class II failed to be killed within the same mice (Fig. 7c). Thus, anti-PD-L1 enhances CD4$^+$ cytotoxic gene networks and restores CD4$^+$ T cell mediated killing during chronic infection, identifying a new mechanism of action of PD-L1 blockade therapy to restore immune function.

Discussion

To date, the role of PD-L1 blockade to restore exhausted antigen-specific $CD4^+$ T cells has been unclear. Our data now demonstrate that anti-PD-L1 therapy in chronic viral infection specifically and cell-intrinsically enhances T_H1 subsets. Indeed, as chronic viral infection persists, T_H1 cells are gradually lost, exasperating CD8 T cell dysfunction[2,6]. In addition to conventional virus-specific $CD4^+$ T cells, we identify that T_H1-phenotype T_{reg} cells are highly responsive to PD-L1 blockade, through expansion, upregulation of suppressive factors and migration into nonlymphoid tissue. T_H1-phenotype T_{reg} cells specifically limit T_H1 responses[40], and consistent with this, we observed that T_{reg} cell depletion during chronic infection preferentially increased T_H1 cells, with minimal effect on T_{FH} cells. The rapid increase in T_{reg} cells by blocking PD-L1 likely reflects feedback inhibition to prevent excessive immunopathology, but likely also explains how they impede CD8 T cell restoration following PD-L1 blockade in chronic infection[41]. Thus, while restoring virus-specific $CD4^+$ T_H1 cells, PD-L1 blockade simultaneously releases counter-measures to cull back this response. PD-L1 blockade did not indiscriminately target $CD4^+$ T cells, but instead the pre-established cycling capacity of specific populations was a major determinant of responding cells, with only limited incorporation of noncycling ones into the therapeutic response. In this way, PD-L1 specifically acts to limit cellular proliferation and makes the highly proliferative T_H1 subsets the prime target in chronic virus infection. Thus, in cases when $CD4^+$ T cells fail to respond to PD-1/L1 blockade therapies, pre-existing cycling antigen-specific subsets may not be present. Yet, it is important to point out that in other disease states where different $CD4^+$ T_H subsets are highly proliferative, these too may be targeted.

$TCF\text{-}1^+$ memory-like CD8 T cells rapidly proliferate and have been shown to be the primary target of PD-L1 blockade[7–13]. On the other hand, the $TCF\text{-}1^+$ $CD4^+$ T cells were only minimally affected by therapy during chronic infection, suggesting that $TCF\text{-}1^+CD4^+$ and $CD8^+$ T cells may function at different ends of the spectrum in response to PD-L1 blockade. $CD4^+$ T_{FH} can respond to immunotherapy in some cancers, particularly breast cancer[42], although these therapies often incorporate anti-CTLA4 which can expand $CD4^+$ T cells[16], enhance T_{FH} cells[43] and indirectly alter $CD4^+$ T cell responses through modulation of T_{reg} cells[44,45]. Anti-PD-1-mediated tuberculosis reactivation in cancer patients exhibits increased *Mtb*-specific $CD4^+$ T_H1, but not T_H17 cells, suggesting that T_H1 cells can indeed respond to anti-PD-1 therapy in contexts other than viral infection[46]. Thus, based on these dichotomies, it will be important to further uncover the basis for disease-specific $CD4^+$ T_H restoration by PD-L1 blockade and how they contribute to disease control (or exasperation).

Considering that PD-1 functions to attenuate TCR signaling[47], it was unexpected that blocking PD-L1 would decrease TCR signaling and downregulate expression of multiple transcription factors and their target genes. However, increased TCR signaling can potentiate CD8 T cell exhaustion[1] and pushes virus-specific $CD4^+$ T cell differentiation toward T_{FH}[2]. Not all transcription factors were decreased following PD-L1 blockade, with specific increases in transcription factors associated with T_H1 programming and differentiation. Thus, blocking PD-L1 and decreasing TCR signaling likely enables the cells to reroute

toward T_H1 amplification and functions; and paradoxically, the decrease in chronic TCR signaling favors restoration of $CD4^+$ T_H1 cells.

Combined with diminishing $CD4^+$ T_H1 responses, we identify the loss of CTL capacity as a $CD4^+$ T cell dysfunction during chronic infection and demonstrate that $CD4^+$ CTL transcriptional networks and killing capacity are completely restored by blocking PD-L1. In this way, not only can anti-PD-L1 enhance $CD4^+$ T_H1 cell help for CD8 T cells, but may also facilitate killing of infected MHC II^+ cells. $CD4^+$ T cells with CTL function have recently been identified in various cancers that can target MHC II^+ tumors, including melanoma and bladder cancer[48,49]. Thus, it is interesting to speculate that anti-PD-1/L1 restoration of cytolytic $CD4^+$ T cell function may be a mechanism of action of these therapies towards MHC II^+ tumors, and may at least partially drive the high response rates to anti-PD-1 therapy in Hodgkin's lymphoma (a B cell tumor) where the tumors are often largely MHC I negative and response rates are correlated with MHC class II expression[14,15]. Although the ability of PD-L1 blockade to restore CD8 CTL killing during chronic viral infection undoubtedly accounts for much of the therapy's efficacy in lowering viral titers, we postulate that $CD4^+$ CTL killing complements and likely further enhances the cytotoxicity potential of anti-PD-L1 therapy, particularly through targeting of virus-infected MHC II^+ antigen presenting cell (APC) populations. Thus, these data high-light that the suppression of $CD4^+$ CTL killing is a $CD4^+$ T cell dysfunction during chronic infection regulated by PD-L1, and that blocking PD-L1 reprograms and functionally restores $CD4^+$ CTL killer cells. Ultimately, these mechanisms have important implications for multiple therapeutic contexts of anti-PD-L1 therapy.

Methods

Mice.

All mice used for experiments were between 6 and 10 weeks old at the initiation of the experiment. Female C57BL/6 mice ($CD45.2^+$) were purchased from the Princess Margaret Cancer Center (PMCC) or The Jackson Laboratory. LCMV-GP_{61-80}-specific $CD4^+$ TCR transgenic (SMARTA; $CD45.1^+$) mice have been described previously[18] and were bred at PMCC. *Pdcd1*$^{-/-}$ mice were purchased from The Jackson Laboratory and subsequently crossed to SMARTA mice to generate PD-$1^{-/-}$ SMARTA mice. These mice were then bred at PMCC. $\beta_2M^{-/-}$ mice and $Foxp3^{DTR}$ mice were purchased from The Jackson Laboratory. All mice were housed under specific pathogen-free conditions. Mice were sex and age matched for experiments. Mouse handling conformed to the experimental protocols approved by the OCI Animal Care Committee at PMCC/University Health Network. No statistical tests were used to predetermine sample sizes. Because the models are well established, sample sizes were chosen based on previous studies of our own and by others in the field[50,51]. Group numbers in each experiment are described in the figure legends.

LCMV infection and T cell adoptive transfer.

Mice were infected i.v. via the retro-orbital sinus with 2×10^6 plaque-forming units (p.f.u.) of LCMV-Cl13. 2×10^5 p.f.u. of LCMV-Armstrong was injected intraperitoneally (i.p.) into mice as a control for the in vivo CTL assay. Virus stocks were prepared and viral titers were

quantified as described previously[18]. LCMV-specific $CD4^+$ SMARTA T cells were isolated from the spleens of transgenic mice by negative selection (StemCell Technologies). Then 3,000 $CD45.1^+$ SMARTA cells (donors) were transferred i.v. into the retro-orbital sinus of naïve $CD45.2^+$ C57BL/6 mice (recipients) that were then infected with LCMV-Cl13 one day later.

In vivo antibody administration.

For in vivo PD-L1 blockade experiments, 250 μg of anti-PD-L1 (10 F.9G2) or isotype control (LTF-2) antibody (BioXcell) was administered i.p. beginning 25 days after cell transfer, and then every 3 days thereafter, as described in the figure legends. Allocation of infected mice to treatment groups was random. Mice were killed 60 h following the first antibody treatment or one day after the third antibody treatment. In some experiments mice were injected i.v. with 3 μg of Thy1.2 fluorescein isothiocyanate antibody and killed 5 min later to examine intravascular versus extravascular localization of cells in the various organs.

FTY720 treatment and Treg cell depletion.

FTY720 was reconstituted in saline and i.p. injected into mice at a dose of 1 mg kg^{-1} daily starting 1 day before the first anti-PD-L1 treatment (that is, day 24 after infection) until the time of death. For T_{reg} depletion mice were injected with 50 μg kg^{-1} of diphtheria toxin at days 23 and 24 after LCMV-Cl13 infection and then every 3 days (day 27 and day 30) until mice were killed on day 33.

Time-of-flight mass cytometry.

The CyTOF antibody panel is listed in Supplementary Table 1. Purified unconjugated antibodies were labeled with metal tags at the SickKids-UHN Flow and Mass Cytometry Facility using the MaxPar Antibody Labeling Kit from Fluidigm. Directly conjugated antibodies were purchased from Fluidigm. All working antibody concentrations were determined by titration.

For staining, single-cell suspensions from individual samples were first stained for 15 min at room temperature (20 °C) with antibodies that did not perform well after fixation. The samples were then washed with PBS and pulsed with 12.5 μM cisplatin (BioVision) in PBS for 1 min at room temperature (20 °C) before quenching with CyTOF staining media (Mg^+/Ca^+ HBSS containing 2% fetal bovine serum (FBS) (Multicell), 10 mM HEPES (pH 7.3; Corning), and FBS underlay. Cells were then fixed for 12 min at rom temperature (20 °C) with transcription factor fixative (eBiosciences) and permeabilized, and individual samples were barcoded before being combined using the 20-Plex Pd Barcoding Kit according to the manufacturer's instructions (Fluidigm). Combined samples were resuspended in staining media containing metal-tagged surface antibodies (Supplementary Table 1) and Fc block for 30 min at 4 °C. Cells were then permeabilized and stained with metal-tagged intracellular antibodies using the Foxp3 Transcription Factor Staining Kit (eBiosciences) according to the manufacturer's instructions. Cells were then incubated overnight in PBS (Multicell) containing 0.3% (w/v) saponin, 1.6% (v/v) paraformaldehyde (Polysciences Inc.) and 1 nM iridium (Fluidigm). Cells were then washed and kept in PBS with 1.6% paraformaldehyde in 4 °C for approximately 1 week until acquisition. Cells

were analyzed on a Helios or Helios2 mass cytometer (Fluidigm) at Sick Kids-UHN Flow and Mass Cytometry Facility. EQ Four Element Calibration Beads (Fluidigm) were used to normalize signal intensity over time on CyTOF software version 6.7. FCS files were manually de-barcoded and analyzed using Cytobank 6.2 (Cytobank, Inc).

Heatmaps were plotted in R using the viridis color package and the gplots package. Arcsinh-transformed median of spectral indices (MSI) values were used to generate the heatmaps. Naïve cell data in heatmaps were obtained from clustering total $CD4^+$ T cells from the same experiments as the virus-specific T cells and graphing MSIs of the naïve cluster defined as PD-1-neg, CD44lo, TCF-1hi and CD127hi. The R implementation of UMAP ($k = 100$) and the PhenoGraph algorithm[52] were used for cluster analysis of arcsinh-transformed CyTOF data. Arcsinh cofactors were manually determined by staining intensity. Marker channels used to cluster each of the cell populations can be found in Supplementary Tables 2 and 3. For clustering, equal sampling of cells was performed on each of the time points based on the lowest common denominator of all groups before clustering. Owing to lower overall numbers of SMARTAs, all cells were used for clustering and the numbers displayed in UMAPs were balanced to accurately display the data. Differential states and differential abundance of clusters were calculated using the limma and edgeR tests respectively, through the “diffcyt” R package and plotted using ggplot2 (ref. [53]). The R package “destiny”[24] was used to make diffusion maps and do the pseudotime analyses of SMARTA cells.

Flow cytometry and intracellular cytokine staining.

Single-cell suspensions were prepared from organs and were stained ex vivo using antibodies to CD4 (GK1.5), CD45.1 (A20), SLAMF1 (TC15-12F12.2), CXCR5 (2G8) and B220 (RA3-6B2), all purchased from BioLegend. Staining for Ki67 (35/Ki-67 RUO) (BD Biosciences) and Nur77 (12.14) (eBiosciences) was performed as directed using the Foxp3 Transcription Factor Staining kit (eBiosciences). Samples were run on a FACS Verse or a FACS Lyric (BD Biosciences) and data analyzed using Flow Jo software (v.9 or v.10; Treestar).

For cytokine quantification, splenocytes were restimulated for 5 h at 37 °C with 5 μg ml^{-1} of MHC class II-restricted LCMV peptide GP_{61-80} in the presence of 50 U ml^{-1} recombinant murine IL-2 and 1 mg ml^{-1} brefeldin A (Sigma). Following the 5 h in vitro restimulation, cells were stained with the fixable viability stain zombie aqua (BioLegend), extracellularly stained as above with $CD4^+$, $CD45.1^+$, and then fixed, permeabilized (BioLegend cytokine staining kit) and stained with IFN-γ (XMG1.2), TNF-α (MP6-XT22) and IL-10 (JES5-16E3) (BioLegend).

Single-cell RNA-sequencing.

SMARTA T cells were transferred into naïve mice that were infected with LCMV-Cl13 a day later. Anti-PD-L1-blocking antibody or isotype control antibody was administered i.p. beginning 25 days after infection and subsequently on day 28 and day 31 for a total of three treatments. Mice were killed following the third treatment (day 33 post infection) and splenocytes from four anti-PD-L1 treated mice or four isotype-treated mice were separately pooled and B cell depleted with anti-CD19 beads (Miltenyi). Single-cell suspensions were

then stained for virus-specific SMARTA T cells using CD4 and CD45.1 and FACSorted on a Moflo Astrios (Beckman Coulter) or a BD FACSAria Fusion cell sorter (Schematic for Sort is shown in Extended Data Fig. 8). Sorted anti-PD-L1 treated and isotype-treated SMARTA cells were then washed twice with PBS + 0.04% BSA and mixed with 10× Genomics Chromium single-cell RNA master mix and loaded onto a 10× chromium chip according to the manufacturer's protocol to obtain single-cell complementary DNA (cDNA). Library generation was performed following the Chromium Single Cell 3′ Reagents Kits v.2 User Guide: CG00052 Rev B. Each library was sequenced on the Illumina HiSeq 2500 platform to achieve an average of 50,000 reads per cell. Sequencing was done at the Princess Margaret Genomics Center. Plasma LCMV titers were measured to confirm that virus was not decreased at the time of death.

For the anti-PD-L1 and isotype-treated SMARTA samples raw sequencing data was processed using Cell Ranger (v.1.3.1, 10× Genomics) to generate expression matrix of RNAs (gene-level counts) for each cell in each sample. Cell Ranger identified 965 cells for the isotype sample and 1,743 cells for the anti-PD-L1 sample. All subsequent downstream analysis was performed in the R statistical programming language using the Seurat (v.3.1.0) package[54]. For various quality control steps involving cell filtering, normalization and removal of technical variation, we merged both samples into a single Seurat object. In total, 179 low-quality cells were filtered out using selected threshold for nUMI ≥ 500, nGene ≥ 200 and <2,500, $\log_{10}$(GenesPerUMI) > 0.80, mitochondrial ratio < 5 and genes with zero counts. The final dataset used for analysis consisted of 2,529 cells (965 cells for isotype and 1,618 cells for anti-PD-L1) and 10,575 genes. The SCTransform function was used to normalize data and regress out factors related to mitochondrial and cell-cycle genes. To identify clusters, we performed an integrated analysis of the cells from isotype and anti-PD-L1 samples using 3,000 highly variable genes and the first 30 principal components. Eight clusters were identified at resolution 0.4. Differential expression analyses for the eight clusters were performed using the MAST function in the Seurat package. Cluster 2 volcano plot was made using the R package Enhancedvolcano.

Predicted upstream regulator analysis of differentially expressed genes was performed by Ingenuity Pathway Analysis software (Qiagen). Gene Set Enrichment Analysis was performed[55,56] on the Enrichment Map gene set "Mouse_GOBP_AllPathways_no_GO_iea_August_01_2017_symbol.gmt"[57] and ImmuneSigDB[55,58] using DE genes preranked by *P* value between anti-PD-L1 and isotype treatments on total cells and in each individual cluster. ImmuneSigDB gene lists were converted from human genes to orthologous mouse genes using Ensembl BioMart[59].

The SCENIC R package (v.1.2.4)[38] was used to assess regulon activity on a cellular level. A regulon is formed of a transcription factor (TF) and its putative direct targets. Briefly, SCENIC defines coexpressed modules based on TF and gene coexpression using the GENIE3 R package (v.1.12.0). Regulons are then defined by excluding indirect targets from the coexpressed modules based on enrichment of DNA TF-binding motifs in targets using the RcisTarget R package (v.1.10.0).

Finally, a regulon activity score (RAS) is calculated for each regulon using the AUCell R package (v.1.13.1) based on the enrichment of a regulon for genes located at the top of a list of all genes ranked by their expression in decreasing order. SCENIC was run on 7,669 genes having at least 75 (3 UMI × 25 (1%) cells) counts per cell, expressed in at least 1% of isotype and anti-PD-L1 treated cells, and available in the mm10 mouse RcisTarget database. SCENIC identified 158 regulons in 2,494 cells out of 3,514 coexpressed modules, of which 107 regulons were active in more than 1% of isotype and anti-PD-L1 treated cells. Regulon RAS average was calculated for cells in each Seurat cluster in isotype and anti-PD-L1 treated groups. The *z*-scores are then calculated by regulon (row normalized). Heatmaps were generated using the pheatmap R package (v.1.0.12).

Bulk RNA-sequencing of CD4$^+$ T_H1 and T_{FH} cells during acute LCMV-Armstrong infection.

SMARTA T cells were transferred into naïve mice that were infected i.p. with 2 × 105 p.f.u. of LCMV-Armstrong a day later. Seven days after infection, mice were killed and splenocytes from ten mice each pooled into three groups for separate replicates and B cell depleted with anti-CD19 beads (Miltenyi). Single-cell suspensions were then stained for virus-specific CD4$^+$ T_H1 and T_{FH} SMARTA cells using CD4$^+$, CD45.1$^+$, SLAMF1 and CXCR5, and FACSorted on a Moflo Astrios (Beckman Coulter) directly into RLT buffer (Qiagen). RNA was isolated using a single-cell RNA purification kit (Norgen Biotech) according to manufacturer's instructions. SMART-Seq v.4 Ultra Low Input RNA Kit for Sequencing (Clontech) was used per manufacturer's instructions for amplification of RNA and subsequent cDNA synthesis. All samples proceeded through NexteraXT DNA Library Preparation (Illumina) using NexteraXT Index Kit V1 or V2 Set A (Illumina) following manufacturer's instructions. A portion of this library pool was sent for sequencing on an Illumina NextSeq HighOutput, single read at the Princess Margaret Genomics Centre. An average of 400 × 10^6 reads were obtained per pool, with an average of 40M reads/sample across the entire data set.

Illumina reads were aligned to the *Mus musculus* GRCm38 genome build 88 (ref. [60]) using HISAT2 (ref. [61]). Alignments were compressed and sorted using SAMtools[62]. The alignments were quantified using HTSeq[63–65] to obtain gene counts. Differential analysis was conducted using edgeR[64,65] with modified code from the rnaseq.wiki protocol[66]. Low-count genes were excluded from the analysis if at least three samples did not have at least one count per million reads mapped (CPM) for that gene. Gene counts were normalized using Trimmed Mean of M values normalization[55,58,67]. Figure was plotted in R using the ggplot2 package[68].

In vivo CTL assay.

Splenocytes from naïve β_2M knockout ($\beta_2M^{-/-}$) mice were isolated for target cells and pulsed with either 5 μg ml^{-1} of LCMV-specific $GP_{61\text{-}80}$ peptide or a nonspecific peptide ($OVA_{323\text{-}339}$) and then respectively labeled with either Tag-it violet proliferation dye (BioLegend) or carboxyfluorescein succinimidyl ester (Sigma). $GP_{61\text{-}80}$ and $OVA_{323\text{-}33}$ labeled $\beta_2M^{-/-}$ splenocytes were mixed at a ratio of 1:1 and 2 million cells were injected into either naïve mice, mice infected for 9 days with LCMV-Armstrong, or mice infected with LCMV-Cl13 that had been administered either their third anti-PD-L1 or isotype

antibody treatment a day earlier (treatment schedule described above). Eighteen hours after target cell transfer, mice were killed and the ratio of specific (Tag-it) to nonspecific (carboxyfluorescein succinimidyl ester) killing of $B220^+$ target cells (MHC II positive) or $CD4^+$ target cells (MHC II negative) was subsequently analyzed by flow cytometry in the spleen. The percentage of specific killing was determined by the following equation: [1 − (ratio of Gp66 to OVA)] ×100.

Data exclusion and blinding.

No data was excluded from this study. On some occasions, SMARTA cells were not detected in recipient mice at the experimental time point, and these were excluded from the analysis (that is, if there are no SMARTA cells, we cannot phenotype or analyze them). Note, this occurred in both isotype- and anti-PD-L1 treated mice, indicating it is not a result of a specific treatment. Data collection and analysis were not performed blind to the conditions of the experiments.

Statistical analysis.

All statistical parameters are described in the figure legends. Student's *t*-tests (two-tailed, unpaired) or one-way ANOVA (two-tailed, unpaired) were performed using GraphPad Prism v.6 (GraphPad Software). Data distribution was assumed to be normal but this was not formally tested. As a result, individual data distribution (individual data points) are shown. In the line and bar graphs the error bars indicate standard deviation (s.d.). In the box and whisker plots the box represents the median and upper and lower quartiles and the whiskers the minimum and maximum values.

Reporting Summary.

Further information on research design is available in the Nature Research Reporting Summary linked to this article.

Extended Data

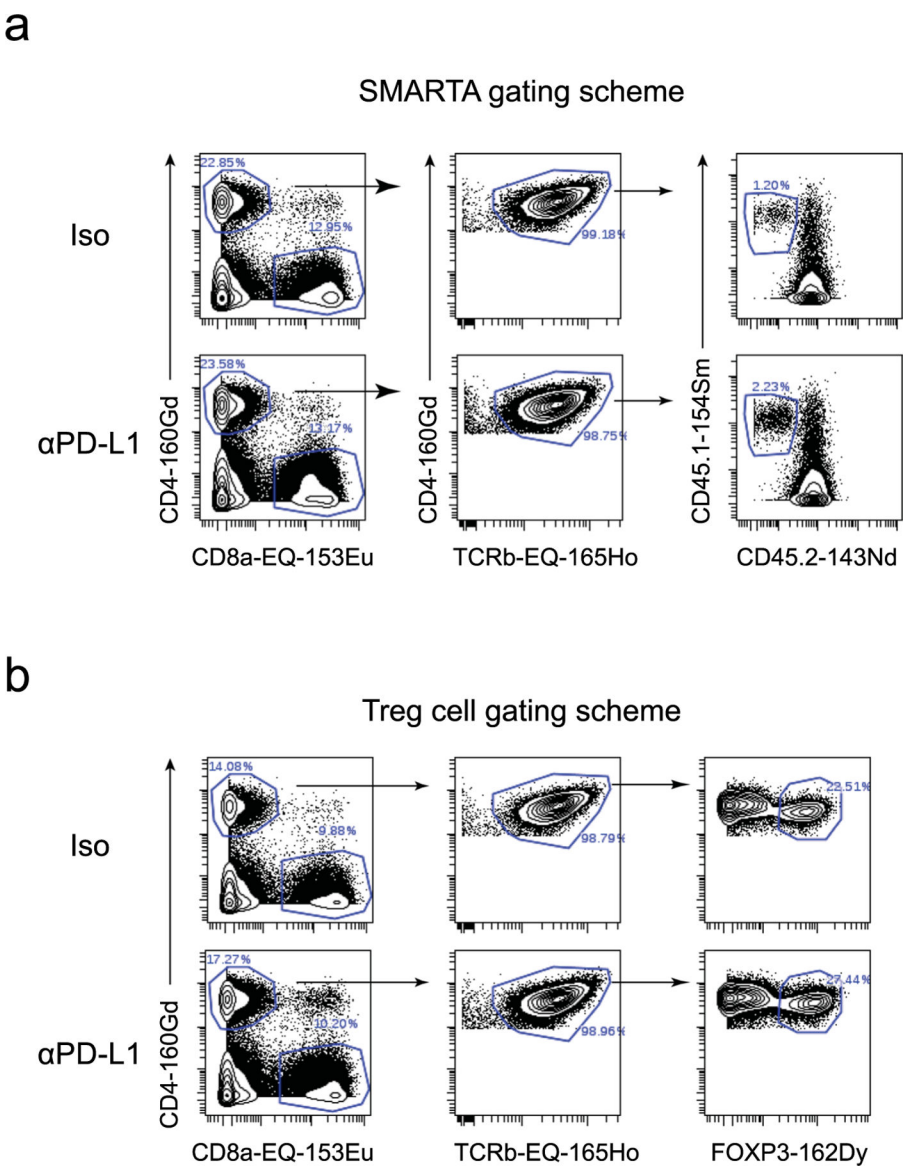

Extended Data Fig. 1 |. CyTOF gating scheme.

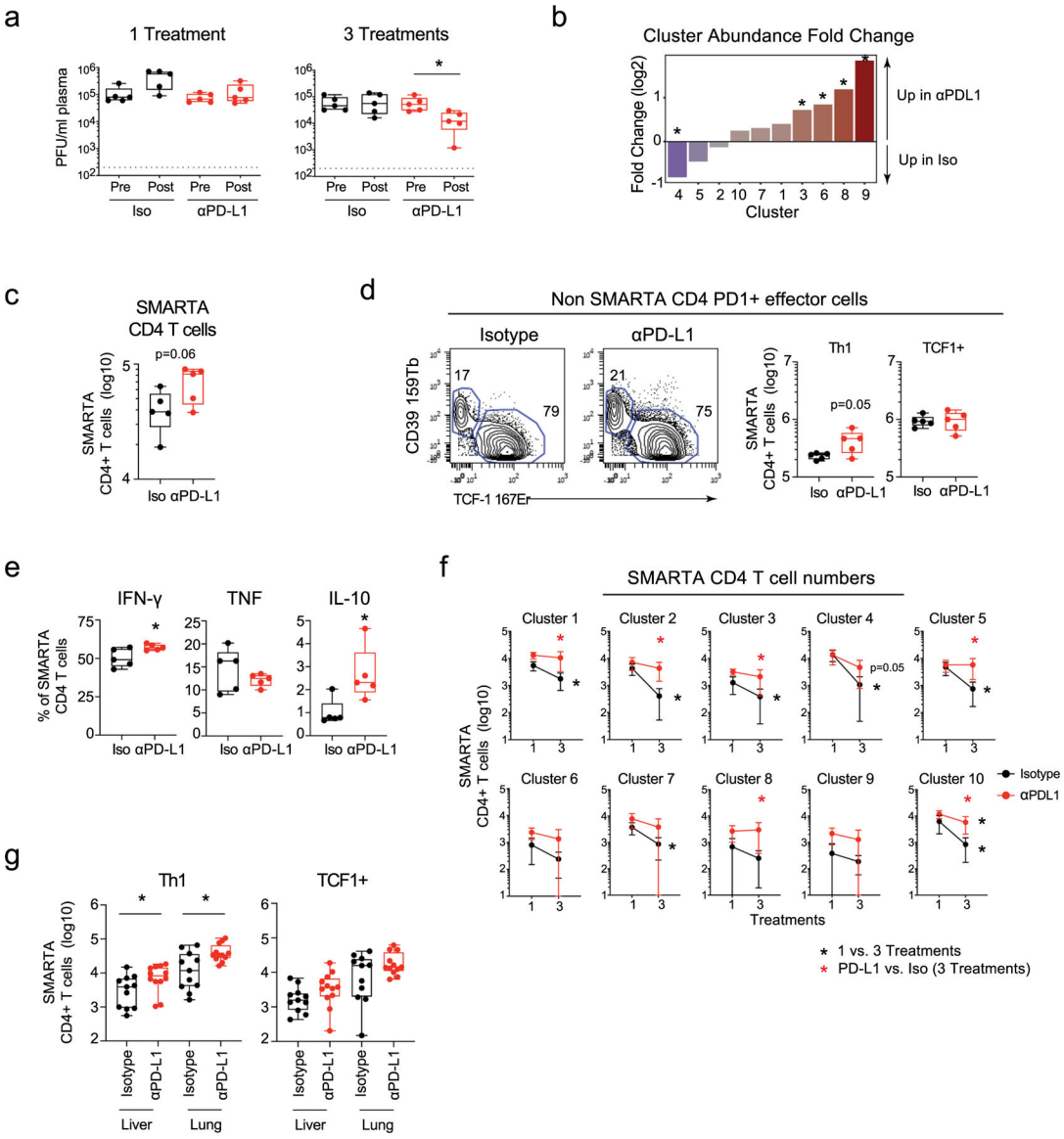

Extended Data Fig. 2 |. Enhancement of virus-specific CD4+ TH1 cells by PD-L1 blockade occurs prior to decreased virus titers.

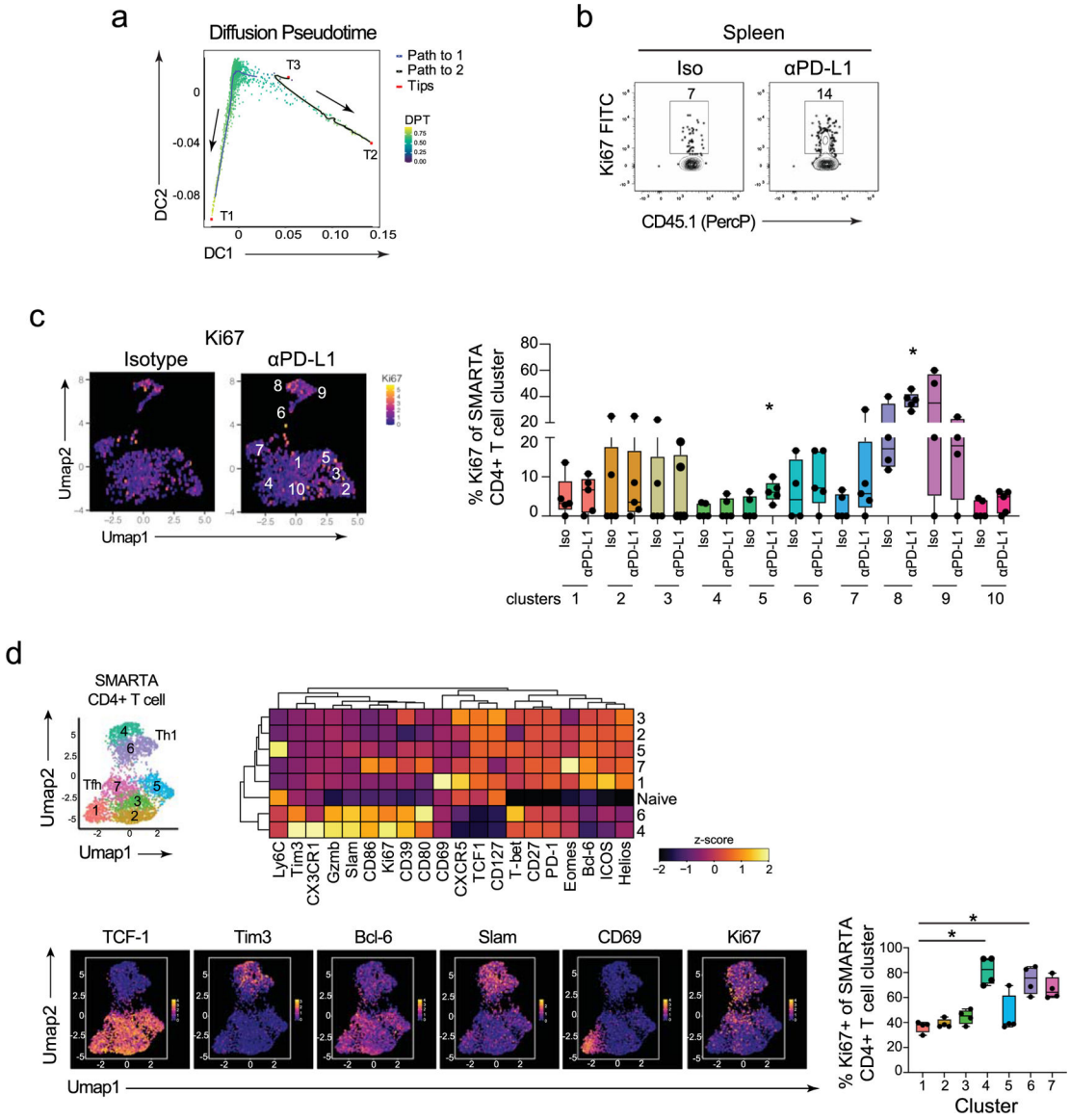

Extended Data Fig. 3 |. Pre-therapy cycling CD4+ SMARTA T cell populations are targets of anti-PD-L1 blockade.

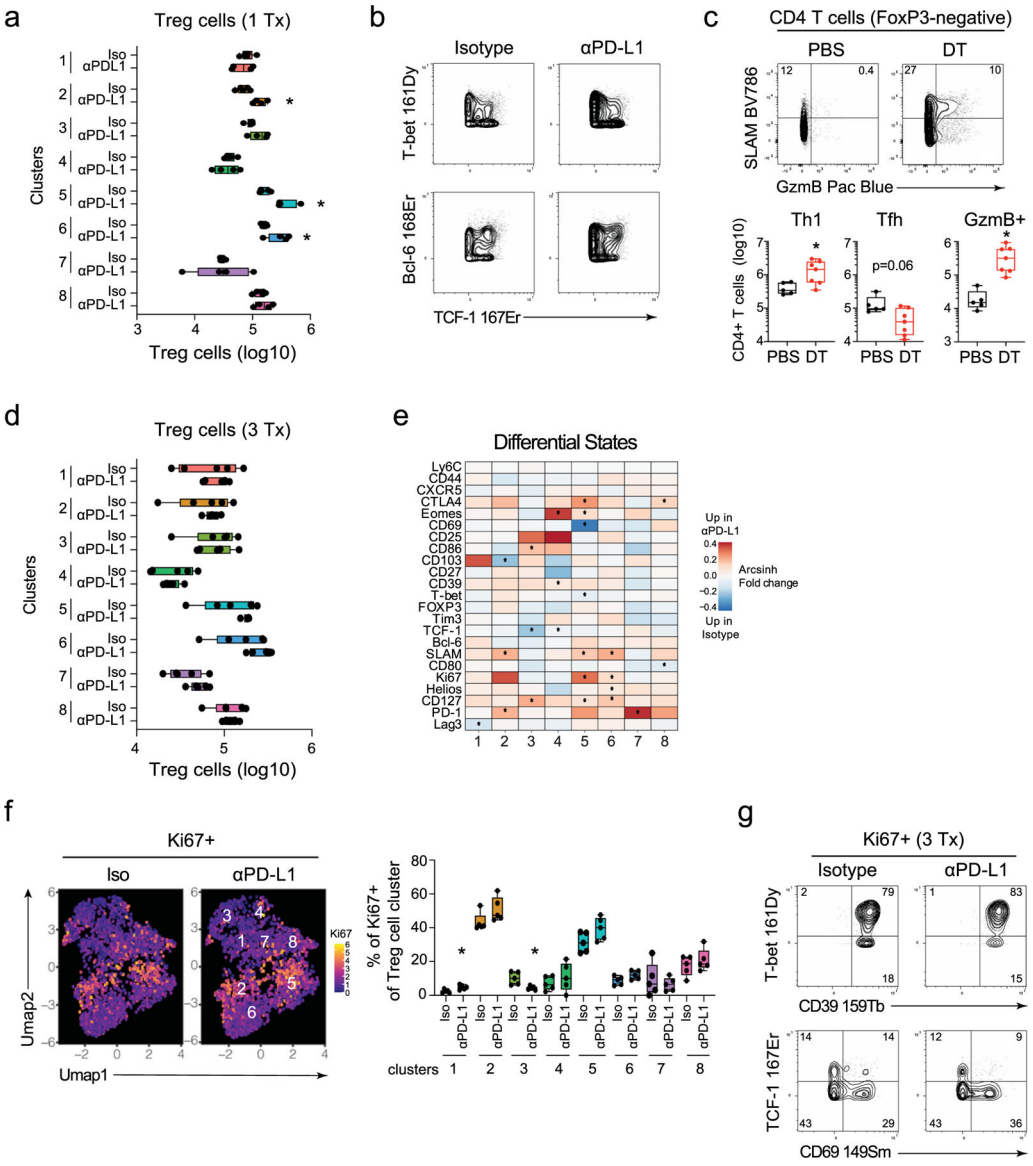

Extended Data Fig. 4 |. PD-L1 blockade targets cycling, TH1-phenotype Treg cells.

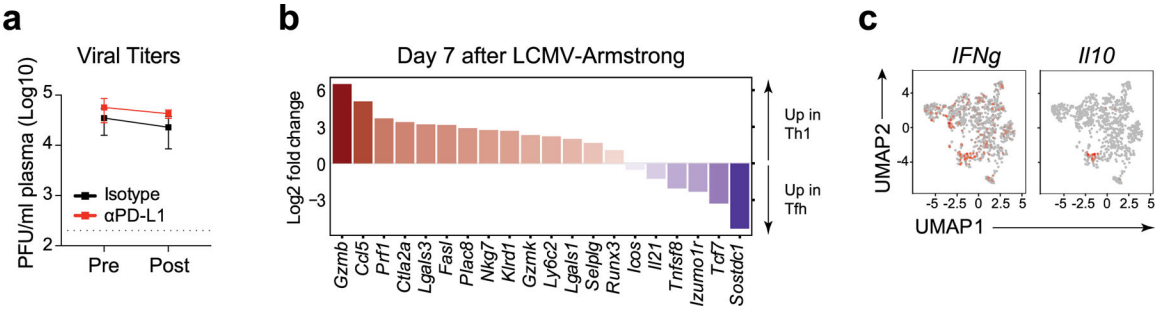

Extended Data Fig. 5 |. Single cell transcriptomic analyses of virus-specific CD4+ T cells following PD-L1 blockade.

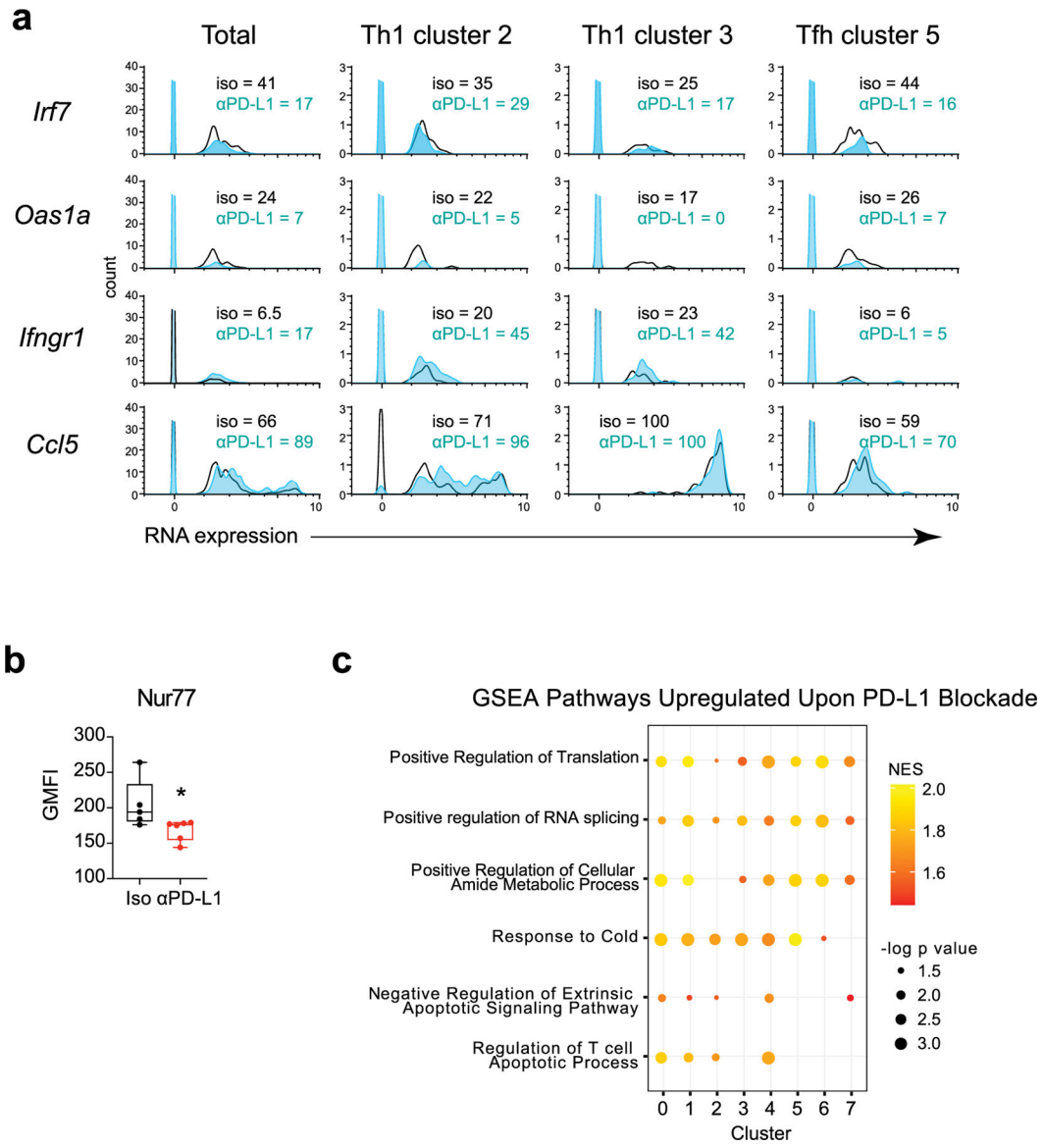

Extended Data Fig. 6 |. Pathway analysis of CD4+ SMARTA T cells following PD-L1 blockade.

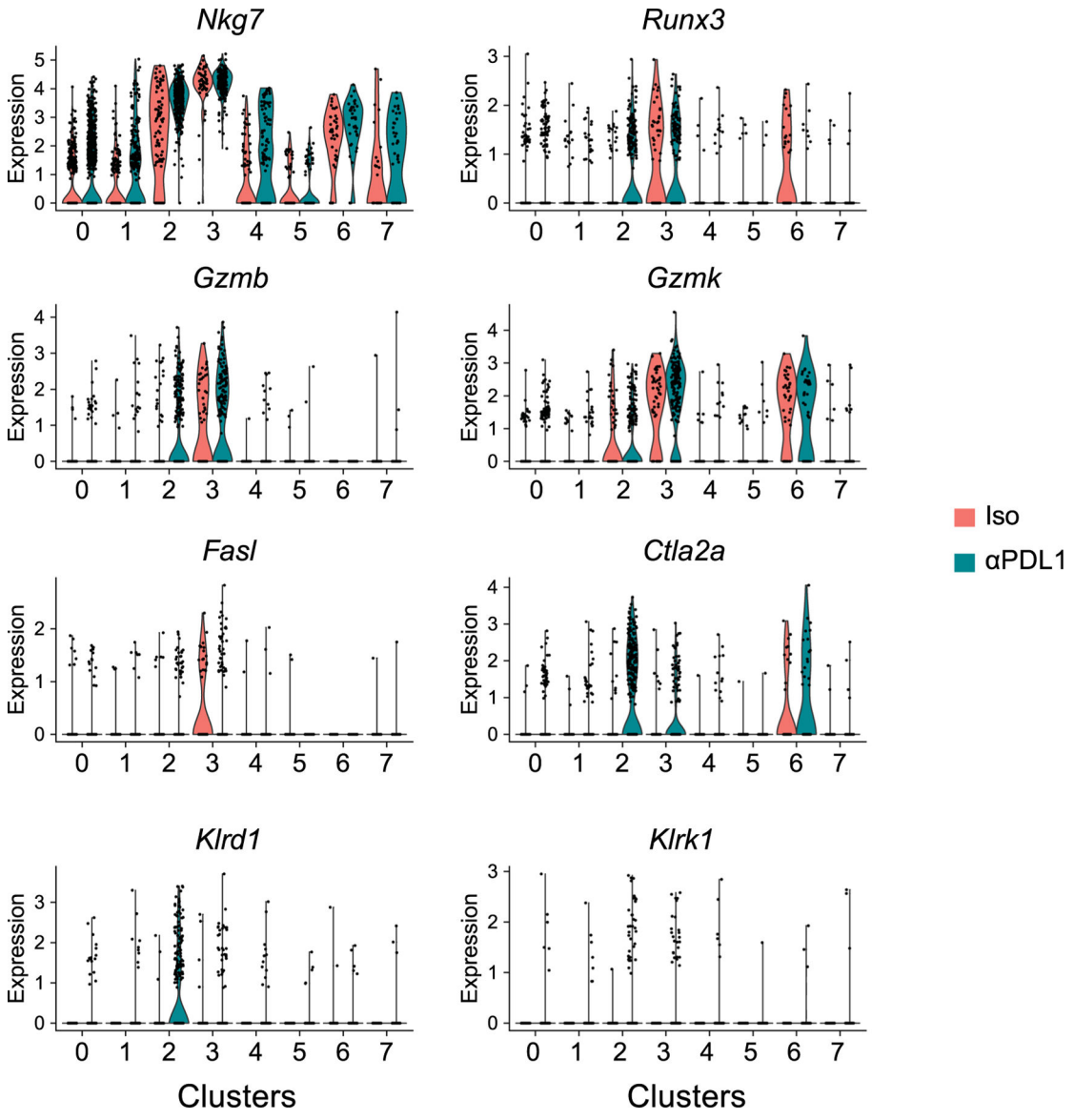

Extended Data Fig. 7 |. Cytotoxic gene expression in all SMARTA clusters from single cell analysis.

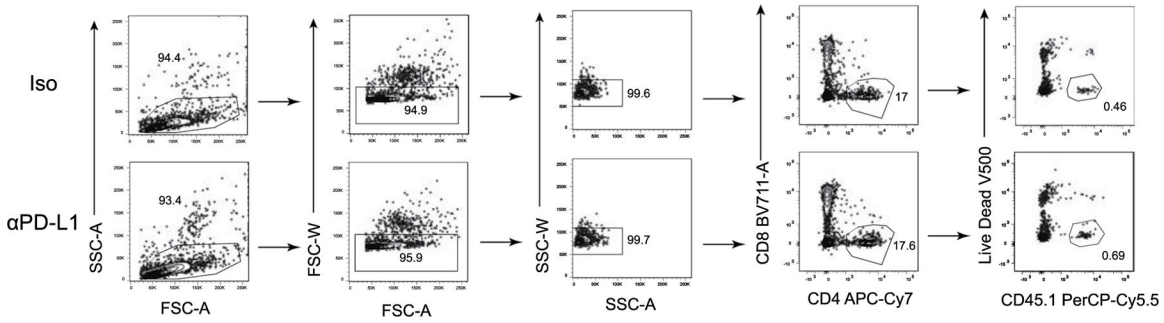

Extended Data Fig. 8 |. Flow gating scheme for sorting.

Supplementary Material

Refer to Web version on PubMed Central for supplementary material.

Acknowledgements

We thank past and present members of the Brooks laboratory for technical help and discussion. This work was supported by the Canadian Institutes of Health Research (CIHR) Foundation Grant FDN148386 (D.G.B.), the National Institutes of Health (NIH) grant AI085043 (D.G.B.), the Scotiabank Research Chair to D.G.B, and a training grant from the Fonds de la Recherche en Santé du Québec (L.M.S.).

Data availability

The RNA-seq data generated in this paper have been deposited in the Gene Expression Omnibus (GEO) database under accession number GSE163345. Source data are provided with this paper.

References

1. McLane LM, Abdel-Hakeem MS & Wherry EJ CD8 T cell exhaustion during chronic viral infection and cancer. Annu. Rev. Immunol 37, 457–495 (2019). [PubMed: 30676822]
2. Fahey LM et al. Viral persistence redirects CD4 T cell differentiation toward T follicular helper cells. J. Exp. Med 208, 987–999 (2011). [PubMed: 21536743]
3. Petrovas C et al. CD4 T follicular helper cell dynamics during SIV infection. J. Clin. Invest 122, 3281–3294 (2012). [PubMed: 22922258]
4. Lindqvist M et al. Expansion of HIV-specific T follicular helper cells in chronic HIV infection. J. Clin. Invest 122, 3271–3280 (2012). [PubMed: 22922259]
5. Feng J et al. Patients with chronic hepatitis C express a high percentage of CD4(+)CXCR5(+) T follicular helper cells. J. Gastroenterol 47, 1048–1056 (2012). [PubMed: 22426636]
6. Snell LM et al. Overcoming CD4 Th1 cell fate restrictions to sustain antiviral CD8 T cells and control persistent virus infection. Cell Rep 16, 3286–3296 (2016). [PubMed: 27653690]
7. Im SJ et al. Defining CD8+ T cells that provide the proliferative burst after PD-1 therapy. Nature 537, 417–421 (2016). [PubMed: 27501248]
8. He R et al. Follicular CXCR5-expressing CD8(+) T cells curtail chronic viral infection. Nature 537, 421–428 (2016).
9. Utzschneider DT et al. T cell factor 1-expressing memory-like CD8(+) T cells sustain the immune response to chronic viral infections. Immunity 45, 415–427 (2016). [PubMed: 27533016]
10. Sade-Feldman M et al. Defining T cell states associated with response to checkpoint immunotherapy in melanoma. Cell 175, 998–1013.e20 (2018). [PubMed: 30388456]
11. Siddiqui I et al. Intratumoral Tcf1(+)PD-1(+)CD8(+) T cells with stem-like properties promote tumor control in response to vaccination and checkpoint blockade immunotherapy. Immunity 50, 195–211.e10 (2019). [PubMed: 30635237]
12. Kurtulus S et al. Checkpoint blockade immunotherapy induces dynamic changes in PD-1(−)CD8(+) tumor-infiltrating T cells. Immunity 50, 181–194.e6 (2019). [PubMed: 30635236]
13. Miller BC et al. Subsets of exhausted CD8(+) T cells differentially mediate tumor control and respond to checkpoint blockade. Nat. Immunol 20, 326–336 (2019). [PubMed: 30778252]
14. Roemer MGM et al. Major histocompatibility complex class II and programmed death ligand 1 expression predict outcome after programmed death 1 blockade in classic Hodgkin lymphoma. J. Clin. Oncol 36, 942–950 (2018). [PubMed: 29394125]
15. Cader FZ et al. A peripheral immune signature of responsiveness to PD-1 blockade in patients with classical Hodgkin lymphoma. Nat. Med 26, 1468–1479 (2020). [PubMed: 32778827]
16. Wei SC et al. Distinct cellular mechanisms underlie anti-CTLA-4 and anti-PD-1 checkpoint blockade. Cell 170, 1120–1133.e17 (2017). [PubMed: 28803728]

17. Huang AC et al. T-cell invigoration to tumour burden ratio associated with anti-PD-1 response. Nature 545, 60–65 (2017). [PubMed: 28397821]
18. Brooks DG, McGavern DB & Oldstone MB Reprogramming of antiviral T cells prevents inactivation and restores T cell activity during persistent viral infection. J. Clin. Invest 116, 1675–1685 (2006). [PubMed: 16710479]
19. Elsaesser H, Sauer K & Brooks DG IL-21 is required to control chronic viral infection. Science 324, 1569–1572 (2009). [PubMed: 19423777]
20. Brooks DG, Teyton L, Oldstone MB & McGavern DB Intrinsic functional dysregulation of CD4 T cells occurs rapidly following persistent viral infection. J. Virol 79, 10514–10527 (2005). [PubMed: 16051844]
21. Xu L et al. The transcription factor TCF-1 initiates the differentiation of T(FH) cells during acute viral infection. Nat. Immunol 16, 991–999 (2015). [PubMed: 26214740]
22. Choi YS et al. LEF-1 and TCF-1 orchestrate T(FH) differentiation by regulating differentiation circuits upstream of the transcriptional repressor Bcl6. Nat. Immunol 16, 980–990 (2015). [PubMed: 26214741]
23. Parish IA et al. Chronic viral infection promotes sustained Th1-derived immunoregulatory IL-10 via BLIMP-1. J. Clin. Invest 124, 3455–3468 (2014). [PubMed: 25003188]
24. Angerer P et al. destiny: diffusion maps for large-scale single-cell data in R. Bioinformatics 32, 1241–1243 (2016). [PubMed: 26668002]
25. Macleod BL et al. A network of immune and microbial modifications underlies viral persistence in the gastrointestinal tract. J. Exp. Med 217, e20191473 (2020). [PubMed: 32880629]
26. Anderson KG et al. Intravascular staining for discrimination of vascular and tissue leukocytes. Nat. Protoc 9, 209–222 (2014). [PubMed: 24385150]
27. Frohlich A et al. IL-21R on T cells is critical for sustained functionality and control of chronic viral infection. Science 324, 1576–1580 (2009). [PubMed: 19478140]
28. Yi JS, Du M & Zajac AJ A vital role for interleukin-21 in the control of a chronic viral infection. Science 324, 1572–1576 (2009). [PubMed: 19443735]
29. Scott AC et al. TOX is a critical regulator of tumour-specific T cell differentiation. Nature 571, 270–274 (2019). [PubMed: 31207604]
30. Khan O et al. TOX transcriptionally and epigenetically programs CD8(+) T cell exhaustion. Nature 571, 211–218 (2019). [PubMed: 31207603]
31. Alfei F et al. TOX reinforces the phenotype and longevity of exhausted T cells in chronic viral infection. Nature 571, 265–269 (2019). [PubMed: 31207605]
32. Paley MA et al. Progenitor and terminal subsets of CD8+ T cells cooperate to contain chronic viral infection. Science 338, 1220–1225 (2012). [PubMed: 23197535]
33. Gabrysova L et al. c-Maf controls immune responses by regulating disease-specific gene networks and repressing IL-2 in CD4(+) T cells. Nat. Immunol 19, 497–507 (2018). [PubMed: 29662170]
34. Wilson EB et al. Blockade of chronic type I interferon signaling to control persistent LCMV infection. Science 340, 202–207 (2013). [PubMed: 23580528]
35. Teijaro JR et al. Persistent LCMV infection is controlled by blockade of type I interferon signaling. Science 340, 207–211 (2013). [PubMed: 23580529]
36. Au-Yeung BB et al. A sharp T-cell antigen receptor signaling threshold for T-cell proliferation. Proc. Natl Acad. Sci. USA 111, E3679–E3688 (2014). [PubMed: 25136127]
37. Fazilleau N, McHeyzer-Williams LJ, Rosen H & McHeyzer-Williams MG The function of follicular helper T cells is regulated by the strength of T cell antigen receptor binding. Nat. Immunol 10, 375–384 (2009). [PubMed: 19252493]
38. Aibar S et al. SCENIC: single-cell regulatory network inference and clustering. Nat. Methods 14, 1083–1086 (2017). [PubMed: 28991892]
39. Ray JP et al. Transcription factor STAT3 and type I interferons are corepressive insulators for differentiation of follicular helper and T helper 1 cells. Immunity 40, 367–377 (2014). [PubMed: 24631156]
40. Levine AG et al. Stability and function of regulatory T cells expressing the transcription factor T-bet. Nature 546, 421–425 (2017). [PubMed: 28607488]

41. Penaloza-MacMaster P et al. Interplay between regulatory T cells and PD-1 in modulating T cell exhaustion and viral control during chronic LCMV infection. J. Exp. Med 211, 1905–1918 (2014). [PubMed: 25113973]
42. Hollern DP et al. B cells and T follicular helper cells mediate response to checkpoint inhibitors in high mutation burden mouse models of breast cancer. Cell 179, 1191–1206.e21 (2019). [PubMed: 31730857]
43. Wang CJ et al. CTLA-4 controls follicular helper T-cell differentiation by regulating the strength of CD28 engagement. Proc. Natl Acad. Sci. USA 112, 524–529 (2015). [PubMed: 25548162]
44. Wing JB, Ise W, Kurosaki T & Sakaguchi S Regulatory T cells control antigen-specific expansion of Tfh cell number and humoral immune responses via the coreceptor CTLA-4. Immunity 41, 1013–1025 (2014). [PubMed: 25526312]
45. Sage PT, Paterson AM, Lovitch SB & Sharpe AH The coinhibitory receptor CTLA-4 controls B cell responses by modulating T follicular helper, T follicular regulatory, and T regulatory cells. Immunity 41, 1026–1039 (2014). [PubMed: 25526313]
46. Barber DL et al. Tuberculosis following PD-1 blockade for cancer immunotherapy. Sci. Transl. Med 11, eaat2702 (2019). [PubMed: 30651320]
47. Yokosuka T et al. Programmed cell death 1 forms negative costimulatory microclusters that directly inhibit T cell receptor signaling by recruiting phosphatase SHP2. J. Exp. Med 209, 1201–1217 (2012). [PubMed: 22641383]
48. Sledzinska A et al. Regulatory T cells restrain interleukin-2- and Blimp-1-dependent acquisition of cytotoxic function by CD4(+) T cells. Immunity 52, 151–166 e156 (2020). [PubMed: 31924474]
49. Oh DY et al. Intratumoral CD4(+) T cells mediate anti-tumor cytotoxicity in human bladder cancer. Cell 181, 1612–1625. e13 (2020). [PubMed: 32497499]
50. Snell LM et al. CD8+ T cell priming in established chronic viral infection preferentially directs differentiation of memory-like cells for sustained immunity. Immunity 49, 678–694.e5 (2018). [PubMed: 30314757]
51. Barber DL et al. Restoring function in exhausted CD8 T cells during chronic viral infection. Nature 439, 682–687 (2006). [PubMed: 16382236]
52. Levine JH et al. Data-driven phenotypic dissection of AML reveals progenitor-like cells that correlate with prognosis. Cell 162, 184–197 (2015). [PubMed: 26095251]
53. Weber LM, Nowicka M, Soneson C & Robinson MD diffcyt: differential discovery in high-dimensional cytometry via high-resolution clustering. Commun. Biol 2, 183 (2019). [PubMed: 31098416]
54. Butler A, Hoffman P, Smibert P, Papalexi E & Satija R Integrating single-cell transcriptomic data across different conditions, technologies, and species. Nat. Biotechnol 36, 411–420 (2018). [PubMed: 29608179]
55. Subramanian A et al. Gene set enrichment analysis: a knowledge-based approach for interpreting genome-wide expression profiles. Proc. Natl Acad. Sci. USA 102, 15545–15550 (2005). [PubMed: 16199517]
56. Mootha VK et al. PGC-1alpha-responsive genes involved in oxidative phosphorylation are coordinately downregulated in human diabetes. Nat. Genet 34, 267–273 (2003). [PubMed: 12808457]
57. Merico D, Isserlin R, Stueker O, Emili A & Bader GD Enrichment map: a network-based method for gene-set enrichment visualization and interpretation. PLoS ONE 5, e13984 (2010). [PubMed: 21085593]
58. Godec J et al. Compendium of immune signatures identifies conserved and species-specific biology in response to inflammation. Immunity 44, 194–206 (2016). [PubMed: 26795250]
59. Kinsella RJ et al. Ensembl BioMarts: a hub for data retrieval across taxonomic space. Database (Oxford) 2011, bar030 (2011). [PubMed: 21785142]
60. Yates A et al. Ensembl 2016. Nucleic Acids Res 44, D710–D716 (2016). [PubMed: 26687719]
61. Kim D, Langmead B & Salzberg SL HISAT: a fast spliced aligner with low memory requirements. Nat. Methods 12, 357–360 (2015). [PubMed: 25751142]
62. Li H et al. The Sequence Alignment/Map format and SAMtools. Bioinformatics 25, 2078–2079 (2009). [PubMed: 19505943]

63. Anders S, Pyl PT & Huber W HTSeq – a Python framework to work with high-throughput sequencing data. Bioinformatics 31, 166–169 (2015). [PubMed: 25260700]

64. Robinson MD, McCarthy DJ & Smyth GK edgeR: a Bioconductor package for differential expression analysis of digital gene expression data. Bioinformatics 26, 139–140 (2010). [PubMed: 19910308]

65. McCarthy DJ, Chen Y & Smyth GK Differential expression analysis of multifactor RNA-Seq experiments with respect to biological variation. Nucleic Acids Res 40, 4288–4297 (2012). [PubMed: 22287627]

66. Griffith M, Walker JR, Spies NC, Ainscough BJ & Griffith OL Informatics for RNA sequencing: a web resource for analysis on the cloud. PLoS Comput. Biol 11, e1004393 (2015). [PubMed: 26248053]

67. Robinson MD & Oshlack A A scaling normalization method for differential expression analysis of RNA-seq data. Genome Biol 11, R25 (2010). [PubMed: 20196867]

68. Wickham H ggplot2: Elegant Graphics for Data Analysis (Springer, 2016).

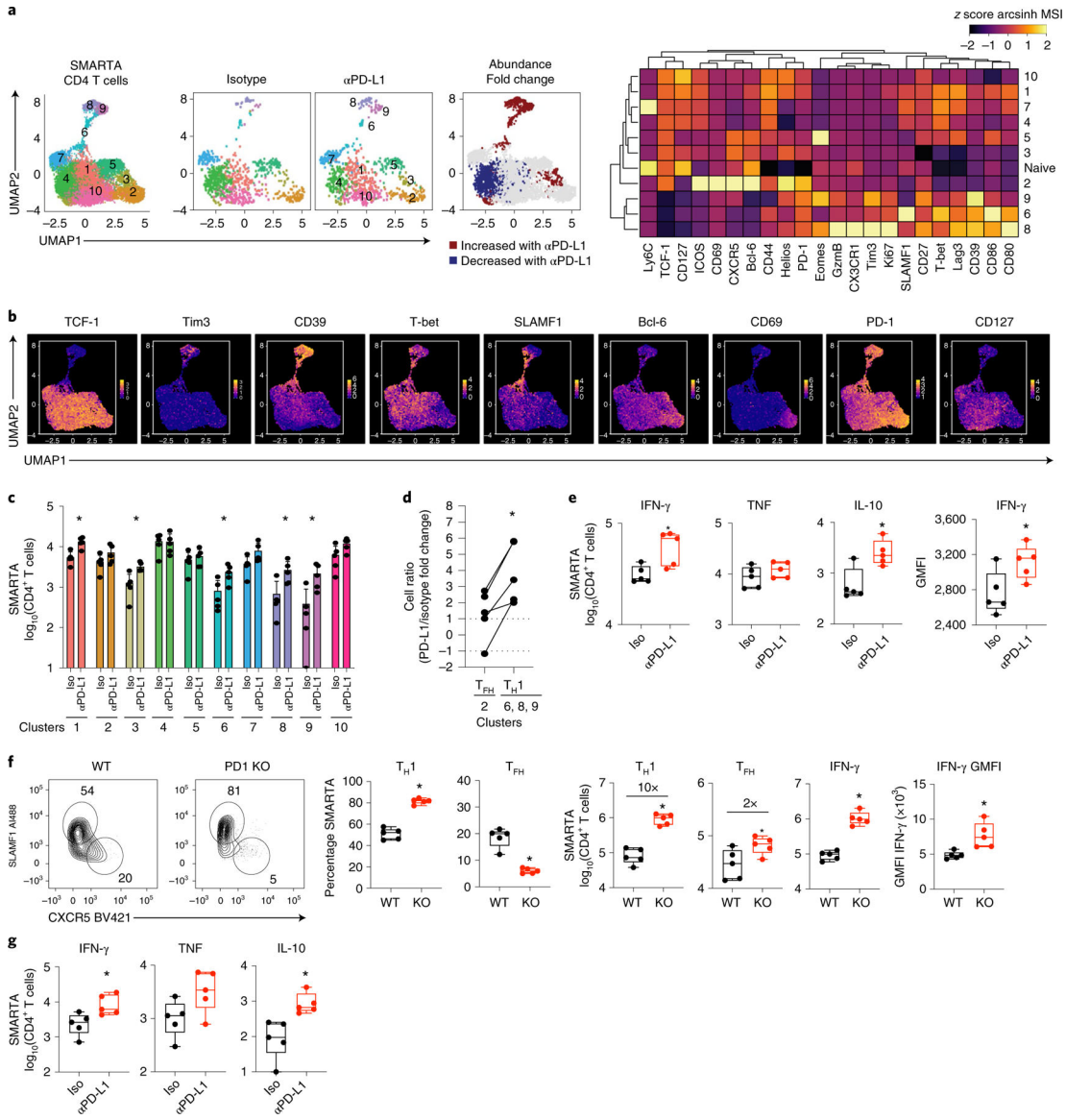

Fig. 1 |. PD-L1 blockade specifically amplifies and functionally enhances CD4$^+$ T_H1 cells.

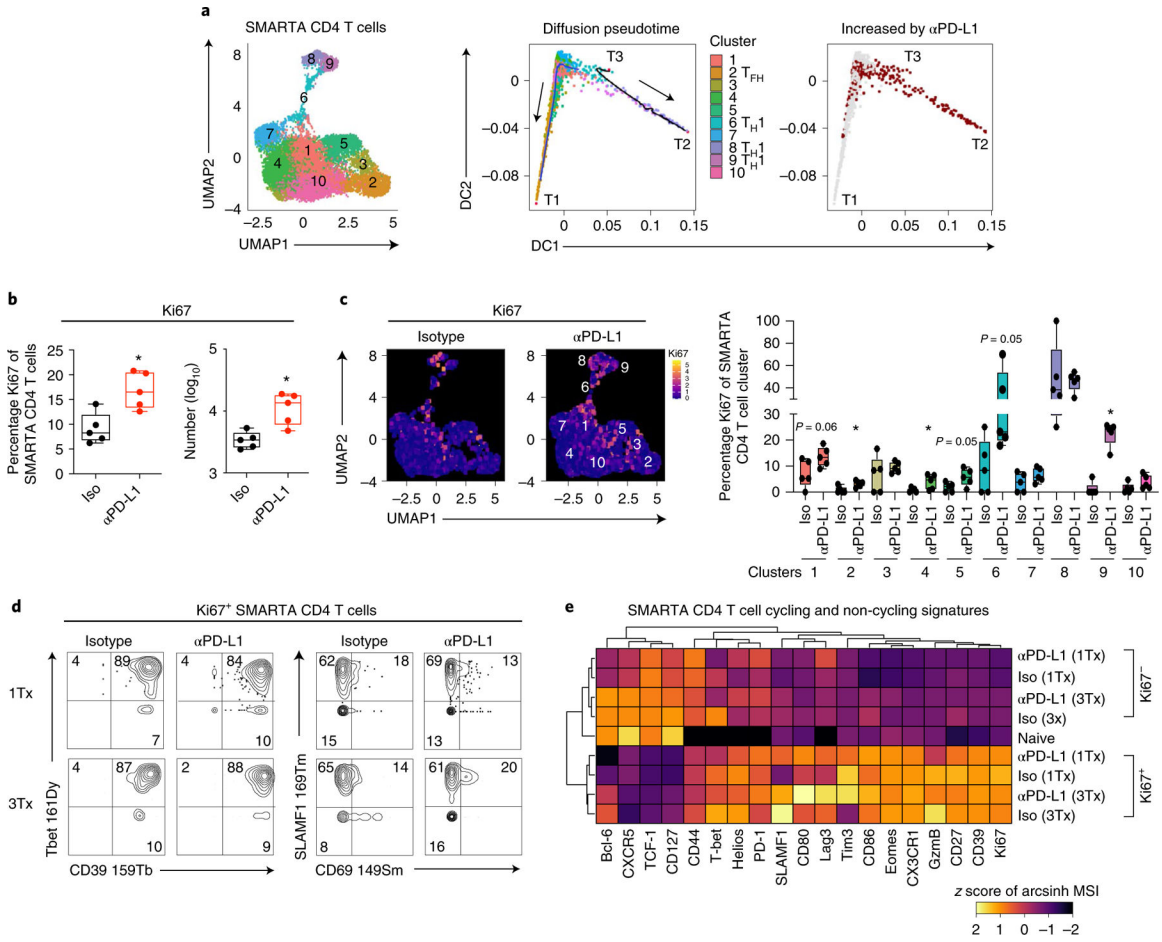

Fig. 2 |. Pretherapy cycling CD4^{+} SMARTA T cells are expanded upon PD-L1 blockade.

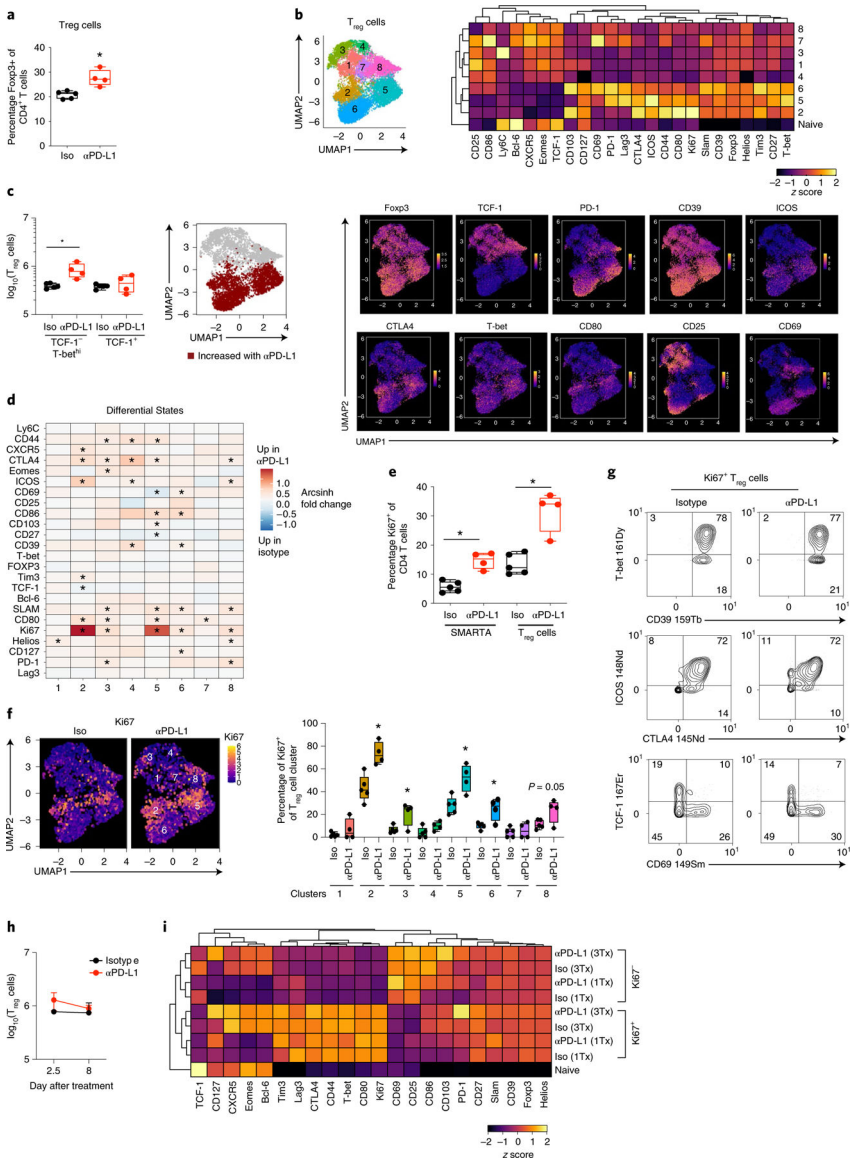

Fig. 3 |. PD-L1 blockade specifically expands and activates T_H1-like T_{reg} cells.

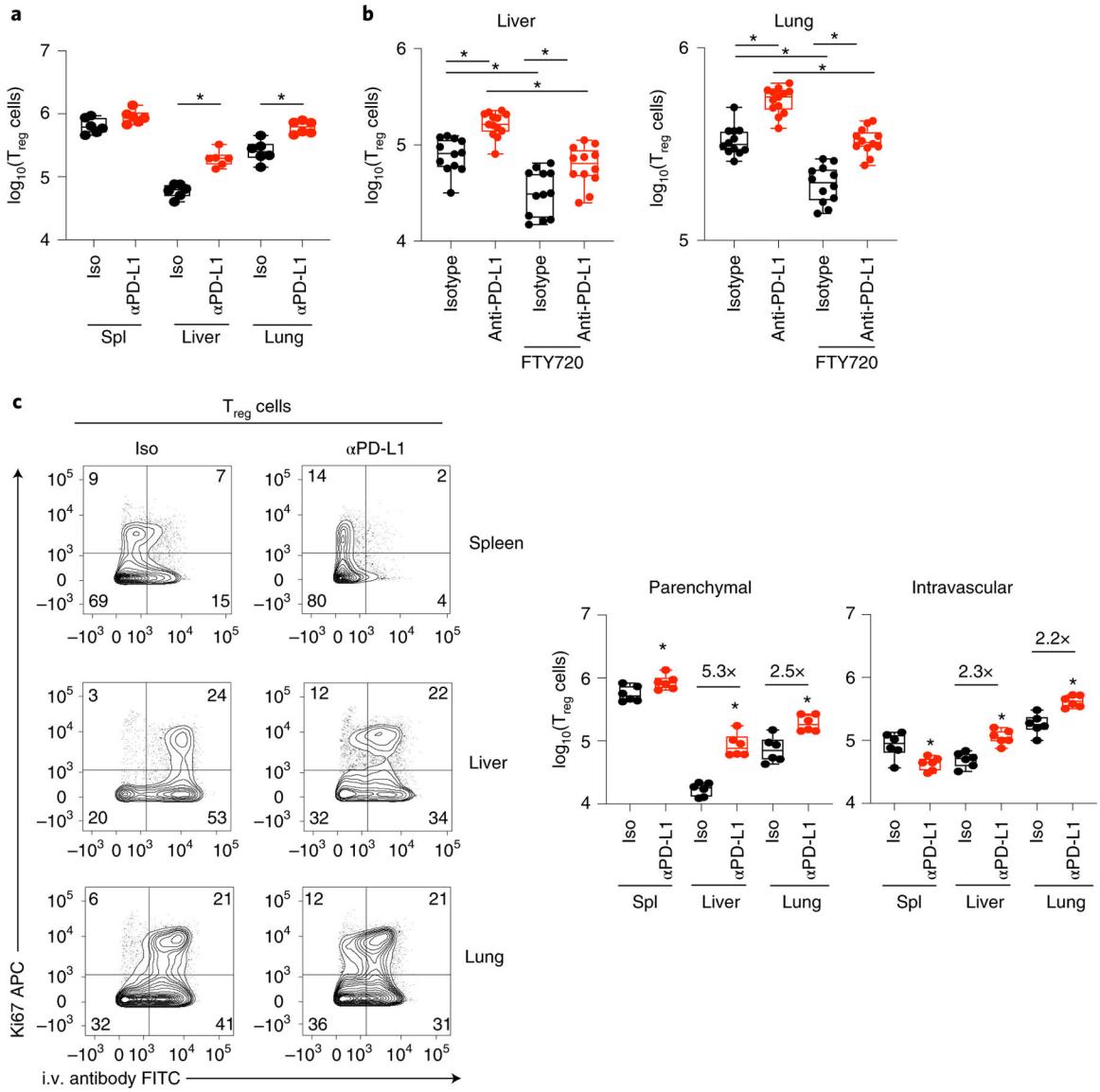

Fig. 4 |. PD-L1 blockade expands and induces tissue infiltration of T_{reg} cells in nonlymphoid organs.

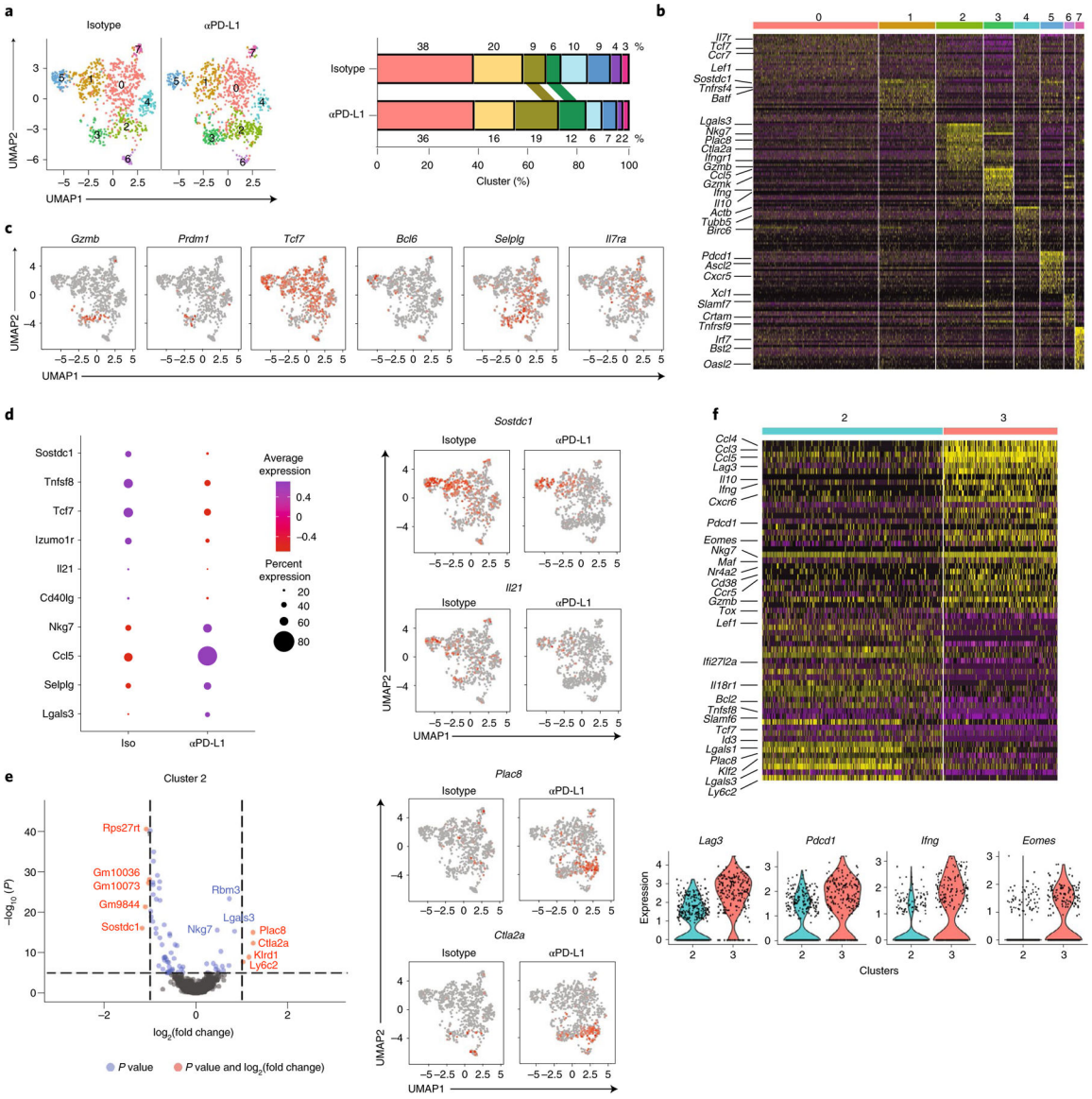

Fig. 5 |. PD-L1 blockade enhances T_H1 gene programs and terminal differentiation of T_H1 cells.

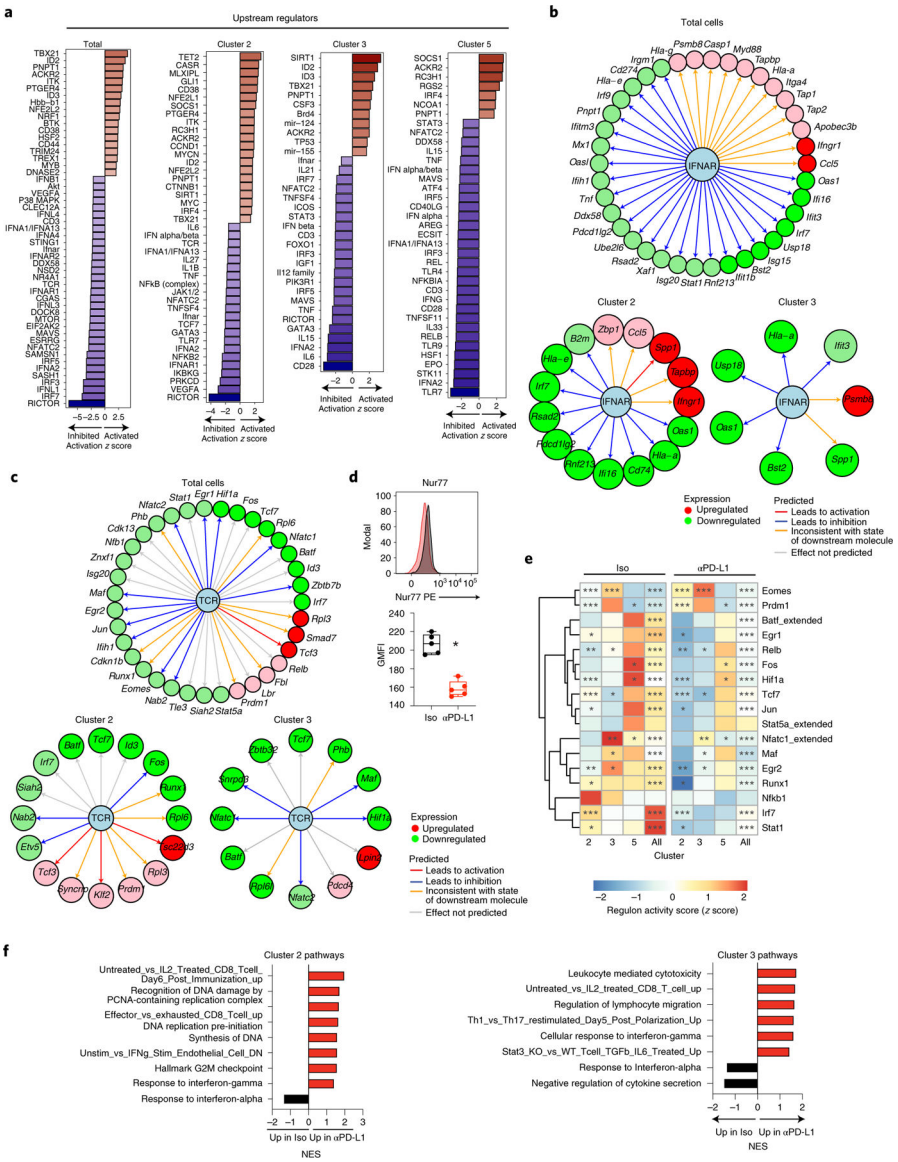

Fig. 6 |. PD-L1 blockade reorients intracellular interferon and TCR signaling.

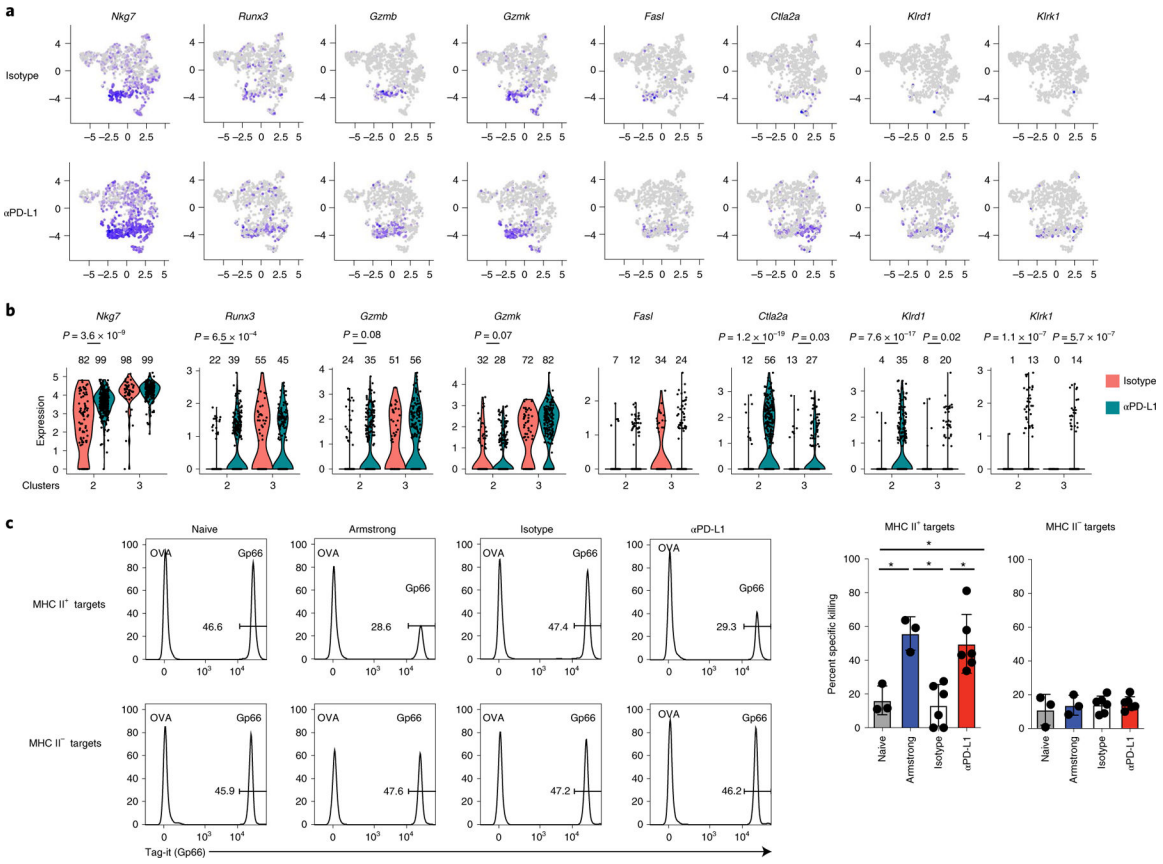

Fig. 7 |. PD-L1 blockade restores virus-specific CD4^{+} CTL function.